

# Journal of Materials Chemistry A

Materials for energy and sustainability

Accepted Manuscript

This article can be cited before page numbers have been issued, to do this please use: M. Lim, Z. Ma, D. Gunawan, Y. Y. Chng, W. Zhong, P. Ramadhany, K. Menon, D. Ruan, P. V. Kumar, A. R. Jalili, R. Amal, R. Daiyan and E. C. Lovell, *J. Mater. Chem. A*, 2026, DOI: 10.1039/D5TA09764A.



This is an Accepted Manuscript, which has been through the Royal Society of Chemistry peer review process and has been accepted for publication.

Accepted Manuscripts are published online shortly after acceptance, before technical editing, formatting and proof reading. Using this free service, authors can make their results available to the community, in citable form, before we publish the edited article. We will replace this Accepted Manuscript with the edited and formatted Advance Article as soon as it is available.

You can find more information about Accepted Manuscripts in the [Information for Authors](#).

Please note that technical editing may introduce minor changes to the text and/or graphics, which may alter content. The journal's standard [Terms & Conditions](#) and the [Ethical guidelines](#) still apply. In no event shall the Royal Society of Chemistry be held responsible for any errors or omissions in this Accepted Manuscript or any consequences arising from the use of any information it contains.

## ARTICLE

# Electrochemical reduction conditioning modified Fe-based catalysts with structural disorders for efficient ammonium production from nitrite reduction

Maggie Lim,<sup>a</sup> Zhipeng Ma,<sup>a</sup> Denny Gunawan,<sup>a</sup> Ying Ying Ch'ng,<sup>a</sup> Wenyu Zhong,<sup>a</sup> Putri Ramadhany,<sup>a</sup> Karan Menon,<sup>a</sup> Daqian Ruan,<sup>a</sup> Priyank Kumar,<sup>a</sup> Ali R. Jalili,<sup>b</sup> Rose Amal,<sup>a</sup> Rahman Daiyan,<sup>\*c</sup> Emma C Lovell<sup>\*a</sup>

Received 00th January 20xx,  
Accepted 00th January 20xx

DOI: 10.1039/x0xx00000x

Electrochemical reduction of  $\text{NO}_2^-$  to  $\text{NH}_4^+$  offers a direct, energy-efficient pathway for sustainable ammonia production by circumventing the rate-determining  $\text{NO}_3^-$ -to- $\text{NO}_2^-$  conversion that constrains traditional  $\text{NO}_3^-$  reduction ( $\text{NO}_3\text{RR}$ ). Herein, we introduce an electrochemical reduction conditioning (ERC) strategy to control  $\text{Fe}_2\text{O}_3$  at different reduction potentials, generating a series of catalysts with tunable  $\text{Fe}^{3+}/\text{Fe}^{2+}/\text{Fe}$  components and lattice strain. Comprehensive *ex situ* and *in situ* characterizations reveal that more negative ERC potentials induce greater structural disorder (i.e., tuned  $\text{Fe}/\text{FeO}/\text{Fe}_2\text{O}_3$  components and pronounced lattice strain) which collectively enhance  $\text{NO}_2^-$  adsorption, water dissociation and hydrogenation of intermediates while suppressing competing  $\text{H}_2$  evolution. Theoretical calculations support that these defective catalyst surface lower the energy barriers for  $\text{NO}_2^-$  adsorption. As a result, the optimized ERC-treated  $\text{Fe}_2\text{O}_3$  catalyst achieves a high  $\text{NH}_4^+$  production rate of  $153 \text{ nmol s}^{-1} \text{ cm}^{-2}$ , Faradaic efficiency of 93% and partial current density of  $\sim 96.5 \text{ mA cm}^{-2}$  at  $-1.0 \text{ V}$  vs RHE. Integration with plasma-generated  $\text{NO}_2^-$ -rich electrolytes further demonstrates stable, decentralized  $\text{NH}_4^+$  production, yielding  $32 \text{ nmol s}^{-1} \text{ cm}^{-2}$ . This work clarifies the mechanistic role of ERC-induced structural disorders in  $\text{NO}_2\text{RR}$  and provides design principles for next-generation metal-oxide catalysts enabling sustainable nitrogen-cycle management.

## 1 Introduction

Ammonia ( $\text{NH}_3$ ), one the world's most produced chemicals, was produced at a scale of 200.7 million tonnes in 2024 and is projected to grow by  $\sim 5\%$  over the next decade.<sup>1,2</sup> It underpins global food security through its dominant use in fertilizers and also serves as a key feedstock for various manufacturing sectors, including pharmaceuticals, plastics, and textiles.<sup>3–6</sup> Recently,  $\text{NH}_3$  has also attracted interest as a hydrogen carrier because it has a higher energy density ( $33.5 \text{ kWh L}^{-1}$  liquid  $\text{NH}_3$ ) than gaseous hydrogen ( $2.4 \text{ kWh L}^{-1}$   $\text{H}_2$ ),<sup>3,7</sup> offering a more efficient way to store and transport hydrogen.<sup>6</sup> It also benefits from its existing, well-developed global production, storage, and transport infrastructure,<sup>6,8</sup> making it central to the emerging global hydrogen economy and Power-to-X pathways.<sup>8</sup> However, over 96% of  $\text{NH}_3$  is still made via the century-old Haber-Bosch (HB) process,<sup>9</sup> which reacts nitrogen and hydrogen gases under extreme conditions, ranging from 400 to 650 °C and from 150 to 200 bar.<sup>10</sup> The hydrogen used in this process is

primarily derived from steam methane reforming, an energy-intensive process that consumes significant amounts of fossil fuels.<sup>11,12</sup> The HB process is estimated to consume  $\sim 1\%$  to  $2\%$  of the world's total energy and contribute to substantial greenhouse gas emissions of  $\sim 1.5\%$  of global carbon dioxide emissions.<sup>11,12</sup> While the HB process has been instrumental in increasing agricultural yields by enabling mass production of  $\text{NH}_3$ , it is economically feasible only on a large, centralized scale.<sup>9,13</sup> This dependence on large-scale, fossil-based production conflicts with the envisioned role of  $\text{NH}_3$  in a low-carbon economy and its potential as a renewable energy carrier for hydrogen, highlighting the urgent need for scalable, decentralized, and renewable-powered alternatives to produce "green"  $\text{NH}_3$ .

The electrochemical conversion of  $\text{NO}_x$  species (i.e.,  $\text{NO}_3^-$  and  $\text{NO}_2^-$ ) to  $\text{NH}_3/\text{NH}_4^+$  using renewable energy has emerged as a promising green alternative to conventional  $\text{NH}_3$  synthesis. The  $\text{NO}_x$  reduction reaction ( $\text{NO}_x\text{RR}$ ) can achieve higher  $\text{NH}_3$  yield and Faradaic efficiency than other proposed green ammonia production methods, such as the direct  $\text{N}_2$  electroreduction reaction (eNRR), which suffers from sluggish kinetics and low selectivity due to the strong  $\text{N}\equiv\text{N}$  bond in  $\text{N}_2$ .<sup>14–17</sup> Another proposed method, Li-mediated  $\text{N}_2$  reduction (Li-NRR), despite achieving high yield and nearly 100% Faradaic efficiency, is limited by high overpotentials, system instability and costly feedstocks (i.e., pure  $\text{N}_2$  and  $\text{H}_2$ , as well as scarce Li metal).<sup>6,8,18</sup>  $\text{NO}_x\text{RR}$  also offers the benefit of closing the  $\text{NO}_x$  loop cycle by

<sup>a</sup> Particles and Catalysis Research Laboratories and School of Chemical Engineering, UNSW Sydney, Sydney, NSW 2052, Australia.

<sup>b</sup> School of Chemistry, UNSW Sydney, Sydney, NSW 2052, Australia.

<sup>c</sup> Particles and Catalysis Research Laboratories and School of Minerals and Energy Resources Engineering, UNSW Sydney, Sydney, NSW 2052, Australia.

Supplementary Information available: Supplementary Figures S1–S20 and supplementary Tables S1–S3. See DOI: 10.1039/x0xx00000x



valorizing pollutants from sources such as power plants, industries and agriculture, producing  $\text{NH}_3$  under mild conditions and thereby contributing to pollution reduction and resource recycling.<sup>8</sup> Moreover,  $\text{NO}_x$  can be synthesized from atmospheric nitrogen using plasma technology,<sup>6,19–21</sup> and when combined with the  $\text{NO}_x\text{RR}$  process, this presents the potential for a self-sustaining, decentralized, green  $\text{NH}_3$  production system powered entirely by renewable energy sources.<sup>6</sup>

Among the  $\text{NO}_x\text{RR}$  pathway, the  $\text{NO}_3^-$  reduction reaction ( $\text{NO}_3\text{RR}$ ) to  $\text{NH}_3/\text{NH}_4^+$  is an eight-electron, multi-step process in which the initial adsorption and deoxygenation of  $\text{NO}_3^-$  to  $\text{NO}_2^-$  has been reported to involve a high-energy barrier, and depending on the catalysts and reaction conditions, may constitute the rate-determining step (RDS).<sup>22–24</sup> These limitations, combined with the relatively weak binding energy of nitrate and nucleophilicity compared with nitrite when interacting with transition metals,<sup>25–28</sup> restrict  $\text{NO}_3\text{RR}$  efficiency. A promising route to improve the viability of  $\text{NH}_3/\text{NH}_4^+$  production is to start directly from  $\text{NO}_2^-$ , which bypasses one of the most energetically demanding steps, requires fewer electrons, thus offering a more direct and energy-efficient pathway to  $\text{NH}_3$ . Achieving this goal requires careful control of the  $\text{NO}_x$  feedstocks. Plasma technology facilitates this by enabling precise control over the relative production of  $\text{NO}_2^-$  and/or  $\text{NO}_3^-$  species in solution, thereby providing a pathway to leverage  $\text{NO}_2^-$  reduction reaction ( $\text{NO}_2\text{RR}$ ) directly. Recent studies have explored the optimization of plasma parameters, such as reactor design, discharge power, operational modes, and plasma activation duration, to enhance  $\text{NO}_x$  yields and fine-tune the  $\text{NO}_2^-/\text{NO}_3^-$  ratios in plasma-activated solutions.<sup>6,21</sup> However, the impact of variations in reaction medium solution conditions (e.g., pH or ion types) on final  $\text{NO}_x$  yields,  $\text{NO}_2^-/\text{NO}_3^-$  ratios, and their subsequent influence on  $\text{NO}_x\text{RR}$  activity remains an area for further investigation.

Despite the advantages of  $\text{NO}_2\text{RR}$ , the factors governing its electrocatalytic activity remain unclear. In particular, catalysts that efficiently reduce  $\text{NO}_3^-$  are not always effective for  $\text{NO}_2^-$  reduction, indicating that the active sites and mechanistic requirements for  $\text{NO}_2\text{RR}$  differ from those of  $\text{NO}_3\text{RR}$ . This discrepancy arises from several factors: (1) the adsorption behaviors of  $\text{NO}_3^-$  and  $\text{NO}_2^-$  driven by differences in their distinct molecular structures and electronic configurations, where catalysts optimized for  $\text{NO}_3^-$  adsorption may not interact as effectively with  $\text{NO}_2^-$ ; (2) differences in electron-proton transfer steps, as  $\text{NO}_3\text{RR}$  involves an additional electron-proton transfer step to convert  $\text{NO}_3^-$  to  $\text{NO}_2^-$ , necessitating different active sites or catalytic properties than those required for the direct reduction of  $\text{NO}_2^-$ ; and (3) the specificity of surface active sites, as those effective for  $\text{NO}_3^-$  binding and reduction may not exhibit similar efficacy for  $\text{NO}_2^-$ . These factors collectively underscore the complexity in designing catalysts capable of efficiently facilitating both  $\text{NO}_3\text{RR}$  and  $\text{NO}_2\text{RR}$ , highlighting the importance of tailored strategies to optimize  $\text{NO}_2\text{RR}$  activity.

Among various transition-metal catalysts, Fe-based materials have shown considerable promise due to their cost-effectiveness and catalytic performance.<sup>29–31</sup>  $\text{Fe}_2\text{O}_3$ , in particular, has been extensively studied for  $\text{NO}_3\text{RR}$ , with well-

characterized mechanisms and RDS. Research indicates that the key RDS for  $\text{Fe}_2\text{O}_3$  catalysts involves the reduction of  $\text{NO}_3^-$  to  $\text{NO}_2^-$ , and that modifying  $\text{Fe}_2\text{O}_3$  by alloying with other transition metals and inducing defects can shift the RDS toward hydrogenation processes.<sup>29,30</sup> These findings underscore the dynamic role of Fe species, where  $\text{Fe}^{3+}$  and  $\text{Fe}^{2+}$  facilitate electron transfer to overcome the high energy barriers in  $\text{NO}_3\text{RR}$ . However, the established catalytic efficiency of  $\text{Fe}_2\text{O}_3$  in  $\text{NO}_3\text{RR}$  does not guarantee similar performance in  $\text{NO}_2\text{RR}$ . The  $\text{NO}_2\text{RR}$  may involve different reaction intermediates and electron transfer dynamics, potentially requiring alternative active site properties or crystal structures.<sup>26,28,32</sup> Consequently, the behavior of  $\text{Fe}_2\text{O}_3$  in  $\text{NO}_2\text{RR}$  remains underexplored, representing a significant knowledge gap in understanding the role of surface chemistry and the electronic interactions that govern  $\text{NO}_2\text{RR}$  activity. Addressing this gap requires detailed investigations into the surface chemistry, electron transport mechanisms, and active site engineering of  $\text{Fe}_2\text{O}_3$  specific to  $\text{NO}_2\text{RR}$ .

Strain engineering has emerged as a promising strategy to enhance catalytic activity by altering crystal structures, inducing lattice distortions, and optimizing active sites.<sup>33,34</sup> In fact, variations in electrochemical reduction conditions can introduce defects that lead to non-stoichiometry, resulting in significant structural changes and creating lattice strains in defect regions.<sup>33,35,36</sup> These strains can modulate the local electronic structure at the catalyst surface, thereby tuning interactions between reaction species and the catalyst.<sup>35</sup> While strain has been shown to enhance catalytic activity in reactions like  $\text{NO}_3\text{RR}$ ,<sup>35,37,38</sup> its specific effects on  $\text{NO}_2\text{RR}$  performance remain poorly understood. In particular, the detailed relationship between strain-induced electronic structure changes and the resulting local physiochemical properties of  $\text{NO}_2\text{RR}$  intermediates on  $\text{Fe}_2\text{O}_3$  catalysts is unclear. Additionally, the influence of variables such as applied potential, on the creation and maintenance of strain has not been thoroughly examined. Furthermore, the operational stability of strained catalysts is not well-documented, as mechanical relaxation or structural changes over time could diminish the benefits of strain. Therefore, mechanistic studies that correlate the degree of strain in  $\text{Fe}_2\text{O}_3$  with its catalytic activity and selectivity in  $\text{NO}_2\text{RR}$  are essential to guide the rational design of strained  $\text{Fe}_2\text{O}_3$  catalysts.

This study employs an electrochemical reduction conditioning (ERC) strategy to control  $\text{Fe}_2\text{O}_3$  catalysts at different reduction potentials, producing a series of catalysts (pristine  $\text{Fe}_2\text{O}_3$ , LR- $\text{Fe}_2\text{O}_3$  and HR- $\text{Fe}_2\text{O}_3$ ) for investigating their activity for  $\text{NO}_2\text{RR}$ -to- $\text{NH}_4^+$  under alkaline conditions. This approach enables a systematic evaluation of how  $\text{Fe}^{3+} \rightarrow \text{Fe}^{2+}/\text{Fe}$  reduction, with tunable  $\text{Fe}/\text{FeO}/\text{Fe}_2\text{O}_3$  components and strain induction, influences  $\text{NO}_2\text{RR}$  performance. Through a suite of *ex situ* and *in situ* characterization techniques, it is revealed that more negative ERC potentials induced greater structural disorder (i.e., tuned  $\text{Fe}/\text{FeO}/\text{Fe}_2\text{O}_3$  components and lattice strain), thereby enhancing  $\text{NO}_2^-$  adsorption, promoting hydrogenation of intermediates and suppressing competing  $\text{H}_2$  evolution. Density functional theory (DFT) calculations on the pristine and



defective hematite surfaces provide further corroboration of these findings. Specifically, the structural defects induced by electrochemical reduction act as bifunctional active sites that simultaneously enhance  $\text{NO}_2^-$  binding and activate water dissociation to provide the surface protons essential for  $\text{NO}_2^-$  reduction process, offering valuable insights for designing next-generation metal-oxide catalysts. These ERC-treated catalysts are further tested in plasma-generated, optimized  $\text{NO}_2^-$ -rich electrolytes obtained by tuning solution pH and plasma reactor voltage to produce  $\text{NH}_4^+$ , showcasing substantial advantages for green ammonium production through bypassing the  $\text{NO}_3^-$ -to- $\text{NO}_2^-$  step and reducing overall energy costs.

## 2 Results and discussion

In this work,  $\text{Fe}_2\text{O}_3$  catalyst powders were prepared through a precipitation-calcination route. Briefly,  $\text{Fe}_2\text{O}_3$  powders were obtained by reacting iron (III) nitrate with sodium carbonate, followed by calcination at 400 °C in flowing air. The resulting  $\text{Fe}_2\text{O}_3$  powder was drop-cast onto carbon fibre paper to prepare the pristine  $\text{Fe}_2\text{O}_3$  electrode. The characteristics of the  $\text{Fe}_2\text{O}_3$  electrodes were further modified using an electrochemical reduction conditioning (ERC) strategy at different applied potentials, with the resulting electrodes denoted as eR- $\text{Fe}_2\text{O}_3$ . Specifically, prior to electrochemical testing, the  $\text{Fe}_2\text{O}_3$  electrodes were pre-treated at reduction potentials of -1.0 V or -2.0 V vs reversible hydrogen electrode (RHE) for 0.5 h. The  $\text{Fe}_2\text{O}_3$  electrodes conditioned at -1.0 V are referred to as Low-Reduction  $\text{Fe}_2\text{O}_3$  (LR- $\text{Fe}_2\text{O}_3$ ), whereas those treated at -2.0 V are designated as High-Reduction  $\text{Fe}_2\text{O}_3$  (HR- $\text{Fe}_2\text{O}_3$ ) (**Experimental Section**).

The  $\text{NO}_2\text{RR}$  activity of pristine  $\text{Fe}_2\text{O}_3$  and eR- $\text{Fe}_2\text{O}_3$  electrodes treated with different ERC potentials (i.e., LR- $\text{Fe}_2\text{O}_3$ , and HR- $\text{Fe}_2\text{O}_3$ ) were evaluated within a two-compartment H-cell system using an electrolyte composed of 0.1 M KOH and 0.1 M  $\text{KNO}_2$  (**Experimental Section**). Across the applied potentials from -0.4 to -1.4 V vs RHE, HR- $\text{Fe}_2\text{O}_3$  exhibits the highest  $\text{NH}_4^+$  production rate and Faradaic efficiency ( $\text{FE}_{\text{NH}_4^+}$ ), followed by LR- $\text{Fe}_2\text{O}_3$ , and lastly, pristine  $\text{Fe}_2\text{O}_3$  (**Figure 1a** and **1b**). Specifically, HR- $\text{Fe}_2\text{O}_3$  achieves its optimal  $\text{NH}_4^+$  production performance at -1.0 V vs RHE, with a production rate and  $\text{FE}_{\text{NH}_4^+}$  of 154  $\text{nmol s}^{-1} \text{cm}^{-2}$  and 93%, respectively. However, at more negative potentials beyond -1.0 V vs RHE, while the  $\text{NH}_4^+$  production rate remains relatively high,  $\text{FE}_{\text{NH}_4^+}$  begins to decrease, indicating increased competition from side reactions and reduced selectivity toward  $\text{NH}_4^+$ .<sup>39–41</sup> The chronoamperometric *i-t* curves depicted in **Figure S1** demonstrate that HR- $\text{Fe}_2\text{O}_3$  maintains the highest partial current density for  $\text{NH}_4^+$  production of ~90.3  $\text{mA cm}^{-2}$  among all samples at  $\text{NO}_2\text{RR}$  applied potential of -1.0 V vs RHE. As a control, to ensure that prolonged ERC treatment does not further change the catalytic activity,  $\text{Fe}_2\text{O}_3$  was ERC-treated for 1 h (double reduction length) instead of 0.5 h at -2.0 V vs RHE to create an HRR- $\text{Fe}_2\text{O}_3$  electrode, which was then tested for its  $\text{NO}_2\text{RR}$  activity under similar operating conditions. As a result, the HRR- $\text{Fe}_2\text{O}_3$  catalyst exhibits essentially identical performance to the HR- $\text{Fe}_2\text{O}_3$  electrode (**Figure S2**), showing overlapping trends in both  $\text{NH}_4^+$  production rate and  $\text{FE}_{\text{NH}_4^+}$

across the applied potentials from -0.4 to 1.4 V vs RHE, with only minor differences within experimental error bars. Hence, this work adopts a 0.5 h ERC pretreatment as the optimal pretreatment condition. Further, the analysis of side products (**Figure S3**) reveals that HR- $\text{Fe}_2\text{O}_3$  generates the least amount of  $\text{H}_2$  (22  $\text{nmol s}^{-1} \text{cm}^{-2}$ ), followed by LR- $\text{Fe}_2\text{O}_3$  (25  $\text{nmol s}^{-1} \text{cm}^{-2}$ ), with pristine  $\text{Fe}_2\text{O}_3$  producing the most (28  $\text{nmol s}^{-1} \text{cm}^{-2}$ ). This suggests that ERC treatment helps suppressing the hydrogen evolution reaction (HER), with more negative reduction treatment potentials leading to greater suppression of HER. Polarization curves (**Figure S4, a-c**) indicate that both LR- $\text{Fe}_2\text{O}_3$  and HR- $\text{Fe}_2\text{O}_3$  exhibit slight improvements in total current densities (*j*) compared to pristine  $\text{Fe}_2\text{O}_3$  across tested potentials in electrolytes of 0.1 M KOH, 0.1 M KOH + 0.1 M  $\text{KNO}_3$ , and 0.1 M KOH + 0.1 M  $\text{KNO}_2$ . For instance, at -1.0 V vs RHE in 0.1 M KOH + 0.1 M  $\text{KNO}_2$  electrolyte (**Figure S4c**), the *j* achieved by pristine  $\text{Fe}_2\text{O}_3$  is -60.1  $\text{mA cm}^{-2}$ , while LR- $\text{Fe}_2\text{O}_3$  and HR- $\text{Fe}_2\text{O}_3$  show improvements of ~16% (-69.9  $\text{mA cm}^{-2}$ ) and ~22% (-73.0  $\text{mA cm}^{-2}$ ), respectively. Similarly, in the electrolytes of 0.1 M KOH only (**Figure S4a**) and 0.1 M KOH + 0.1 M  $\text{KNO}_3$  (**Figure S4b**), at -1.0 V vs RHE, HR- $\text{Fe}_2\text{O}_3$  achieves the highest *j* of ~-38.2 and -70.7  $\text{mA cm}^{-2}$ , representing improvements of ~15% and 13% over pristine  $\text{Fe}_2\text{O}_3$  (-33.1 and -62.8  $\text{mA cm}^{-2}$ , respectively). LR- $\text{Fe}_2\text{O}_3$  shows modest improvements of ~10% (~-36.4  $\text{mA cm}^{-2}$ ) and ~6.8% (-67.1  $\text{mA cm}^{-2}$ ) over pristine  $\text{Fe}_2\text{O}_3$  in the same electrolytes. These results suggest that ERC-conditioned  $\text{Fe}_2\text{O}_3$  catalysts exhibit slightly enhanced intrinsic activity overall. However, the difference in *j* between LR- $\text{Fe}_2\text{O}_3$  and HR- $\text{Fe}_2\text{O}_3$  is minor. A more pronounced difference is observed in the partial current density for  $\text{NH}_4^+$  production ( $j_{\text{NH}_4^+}$ ) under the electrolyte condition of 0.1 M KOH + 0.1 M  $\text{KNO}_2$  (**Figure 1c**). Compared to pristine  $\text{Fe}_2\text{O}_3$ , which achieves  $j_{\text{NH}_4^+}$  of ~-49.1  $\text{mA cm}^{-2}$ , LR- $\text{Fe}_2\text{O}_3$  and HR- $\text{Fe}_2\text{O}_3$  show significant improvements of ~24% (-61.0  $\text{mA cm}^{-2}$ ) and ~37% (-67.4  $\text{mA cm}^{-2}$ ), respectively. This indicates that the more negative ERC (HR) potential enhances selectivity toward  $\text{NH}_4^+$  production, with both treated catalysts showing a marked improvement in  $j_{\text{NH}_4^+}$  over pristine  $\text{Fe}_2\text{O}_3$ . As a control, to compare the activity between  $\text{NO}_2\text{RR}$  and  $\text{NO}_3\text{RR}$ , pristine  $\text{Fe}_2\text{O}_3$  and HR- $\text{Fe}_2\text{O}_3$  electrodes were also used to conduct electrocatalytic  $\text{NO}_3\text{RR}$  in an electrolyte containing 0.1 M KOH and 0.1 M  $\text{KNO}_3$ . The results, presented in **Figure S5**, clearly demonstrate that both electrodes produce greater  $\text{NH}_4^+$  and  $\text{FE}_{\text{NH}_4^+}$  in  $\text{NO}_2\text{RR}$  than in  $\text{NO}_3\text{RR}$ , with HR- $\text{Fe}_2\text{O}_3$  consistently outperforming pristine  $\text{Fe}_2\text{O}_3$  in nitrate and nitrite reduction. Specifically, for  $\text{NO}_2\text{RR}$ , HR- $\text{Fe}_2\text{O}_3$  achieves a peak  $\text{FE}_{\text{NH}_4^+}$  of 93% at -1.0 V vs RHE, with an  $\text{NH}_4^+$  production rate of ~154  $\text{nmol s}^{-1} \text{cm}^{-2}$ . This represents a 31% improvement in productivity and 15% increase in  $\text{FE}_{\text{NH}_4^+}$  compared to pristine  $\text{Fe}_2\text{O}_3$  (~118  $\text{nmol s}^{-1} \text{cm}^{-2}$  and 81% at -1.0 V vs RHE). For  $\text{NO}_3\text{RR}$ , HR- $\text{Fe}_2\text{O}_3$  also outperforms pristine  $\text{Fe}_2\text{O}_3$ , achieving an  $\text{NH}_4^+$  production rate of ~101  $\text{nmol s}^{-1} \text{cm}^{-2}$  at -1.0 V vs RHE, corresponding to a 5% improvement over pristine  $\text{Fe}_2\text{O}_3$  (~96  $\text{nmol s}^{-1} \text{cm}^{-2}$ ). Importantly, the results indicate that the improvements in  $\text{NH}_4^+$  production are more pronounced in  $\text{NO}_2\text{RR}$  than in  $\text{NO}_3\text{RR}$  following the ERC treatment. This suggests that the ERC-treated  $\text{Fe}_2\text{O}_3$  catalysts are more surface-active for  $\text{NO}_2\text{RR}$  than  $\text{NO}_3\text{RR}$ ,



and that ERC treatment yields better performance enhancements for NO<sub>2</sub>RR than for NO<sub>3</sub>RR.

Electrochemical impedance spectroscopy (EIS) was employed to

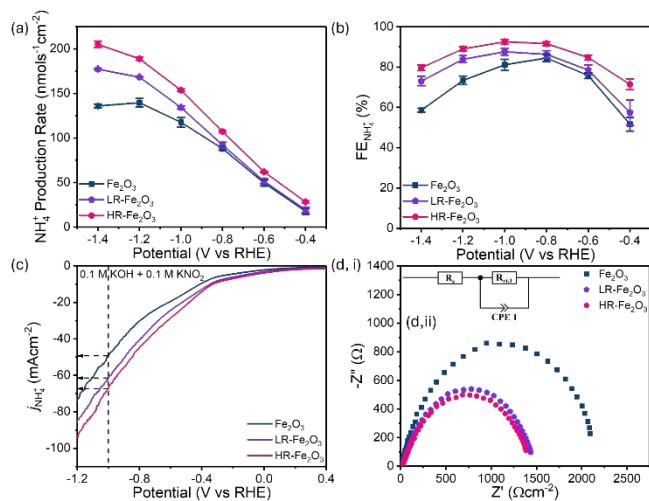


**Fig. 1** NO<sub>2</sub>RR-to-NH<sub>4</sub><sup>+</sup> production performances of Fe<sub>2</sub>O<sub>3</sub>, LR-Fe<sub>2</sub>O<sub>3</sub>, and HR-Fe<sub>2</sub>O<sub>3</sub> electrodes across an applied potential range of -1.4 to -0.4 V vs RHE: (a) NH<sub>4</sub><sup>+</sup> production rate and (b) Faradaic efficiency (FE<sub>NH<sub>4</sub><sup>+</sup></sub>). (c) Partial current density for NH<sub>4</sub><sup>+</sup> (j<sub>NH<sub>4</sub><sup>+</sup></sub>) of all electrodes in 0.1 M KOH + 0.1 M KNO<sub>2</sub>. (d, i) Nyquist plot and its corresponding (d, ii) equivalent circuit of Fe<sub>2</sub>O<sub>3</sub>, LR-Fe<sub>2</sub>O<sub>3</sub>, and HR-Fe<sub>2</sub>O<sub>3</sub> electrodes.

understand charge-transfer resistances during the NO<sub>2</sub>RR process. The Nyquist plots (Figure 1d) display a single semicircle for all electrodes, indicative of the charge transfer resistance at the electrode/electrolyte interface.<sup>42,43</sup> Notably, the radius of the semicircle decreases as the reduction treatment potential becomes more negative. Coupled with the equivalent circuit modeling (Figure 1d, ii), the results reveal that HR-Fe<sub>2</sub>O<sub>3</sub> exhibits a ~ 35% lower charge transfer resistance compared to pristine Fe<sub>2</sub>O<sub>3</sub> (1.4 kΩ vs 2.2 kΩ), while LR-Fe<sub>2</sub>O<sub>3</sub> shows a ~ 21% reduction (1.8 vs 2.2 kΩ). These results demonstrate that the electrode preconditioned at a more negative reduction potential has reduced charge transfer resistance, thereby benefiting NH<sub>4</sub><sup>+</sup> production rates and selectivity during NO<sub>2</sub>RR.<sup>8</sup> Additionally, the electrochemically active surface area (ECSA) of the catalysts was determined using cyclic voltammetry and double-layer capacitance methods (CDL) (Figures S6-7).<sup>44,45</sup> The results (Table S1) indicate that ECSA does not exhibit a significant difference (ranging from 5.1 to 6.7 cm<sup>2</sup>). Therefore, the changes in performance are likely influenced by other factors, such as modifications in structure and/or surface chemistry (e.g., coordination environment and defects) as a result of ERC treatment.

To investigate the surface chemistry of the catalysts and understand how NH<sub>4</sub><sup>+</sup> production performance is influenced by ERC treatments, X-ray photoelectron spectroscopy (XPS) measurements were performed on all as prepared electrodes (pristine Fe<sub>2</sub>O<sub>3</sub>, LR-Fe<sub>2</sub>O<sub>3</sub>, and HR-Fe<sub>2</sub>O<sub>3</sub>). Figure 2a presents the high-resolution Fe 2p XPS spectra, which show doublet peaks at ~ 724.1 and 710.8 eV corresponding to Fe 2p<sub>1/2</sub> and Fe 2p<sub>3/2</sub>, respectively.<sup>46</sup> These are typical binding energies for Fe<sup>3+</sup> indicating Fe<sub>2</sub>O<sub>3</sub>.<sup>46</sup> In addition, a satellite peak at ~ 720.0 eV, characteristic of α-Fe<sub>2</sub>O<sub>3</sub>,<sup>46</sup> is observed. Notably, a positive shift

of ~ 0.4 to 0.7 eV in the Fe 2p peaks is observed for LR-Fe<sub>2</sub>O<sub>3</sub> and HR-Fe<sub>2</sub>O<sub>3</sub> compared to pristine Fe<sub>2</sub>O<sub>3</sub>, respectively, suggesting possible changes in the coordination environment and/or induction of strain following ERC.<sup>47-50</sup> The fitted Fe 2p spectra (Figure S8, a-c) demonstrate that increasing the ERC potential (more negative) results in a further reduction of Fe species. Specifically, when the electrode is preconditioned at a low reduction (LR) potential (-1.0 V vs RHE), 19.2% of Fe<sub>2</sub>O<sub>3</sub> in LR-Fe<sub>2</sub>O<sub>3</sub> is reduced to Fe and FeO, accounting for 2.6% and 16.6% (Figure S8b), respectively. At a more negative (high reduction, HR) treatment potential (-2.0 V vs RHE), HR-Fe<sub>2</sub>O<sub>3</sub> experiences a slightly larger portion of Fe<sub>2</sub>O<sub>3</sub> (23.5%) being reduced to Fe and FeO, comprising 2.8% and 20.7% (Figure S8c), respectively. The emergence of these FeO and metallic Fe on the catalyst surface shows the tuneable FeO/Fe/Fe<sub>2</sub>O<sub>3</sub> components with different ERC treatment potentials, these reconstructed metal and metal oxide species likely provide complementary active sites for NO<sub>2</sub>RR activity, as reported in prior NO<sub>3</sub>RR studies.<sup>29,30,51</sup> To further understand the Fe oxidation states, *ex situ* and *in situ* X-ray absorption near-edge structure (XANES) spectra of LR-Fe<sub>2</sub>O<sub>3</sub> and HR-Fe<sub>2</sub>O<sub>3</sub> catalysts were evaluated (Figure S9). The XANES spectra were compared with the reference compound spectra (metallic Fe and Fe<sub>2</sub>O<sub>3</sub>). The results clearly show that the absorption edge positions and white-line intensities of both catalysts lie between those of metallic Fe and Fe<sub>2</sub>O<sub>3</sub> reference, indicating that both LR-Fe<sub>2</sub>O<sub>3</sub> and HR-Fe<sub>2</sub>O<sub>3</sub> catalysts possessed mixed oxidation states between metallic Fe and Fe<sub>2</sub>O<sub>3</sub>, corroborating the results from XPS analyses. Furthermore, under experimental conditions of open-circuit potential and -1.0 V vs RHE in 0.1 M KOH with 0.1 M KNO<sub>2</sub> electrolyte, the *in situ* XANES spectra remain consistent with the *ex situ* observations, confirming that these mixed-valence Fe species are maintained during operation. In addition, *in situ* PD spectra (Figure S10) were collected at the same conditions as the *in situ* XANES to further substantiate the coexistence of Fe and Fe oxide species in LR-Fe<sub>2</sub>O<sub>3</sub> and HR-Fe<sub>2</sub>O<sub>3</sub>. The LR-Fe<sub>2</sub>O<sub>3</sub> catalyst exhibits diffraction features at 21.3, 24.8, and 35.4°, assignable to Fe (011) (#96-230-0201), Fe<sub>2</sub>O<sub>3</sub> (024) (#96-210-1168), and FeO (113) (#96-900-8637) throughout the 30 min reaction, respectively, while an additional FeO (222) (#96-900-8637) reflection at 36.3° emerged during electrolysis. Similarly, the HR-Fe<sub>2</sub>O<sub>3</sub> catalysts show characteristic reflections at 21.3, 31.5, 24.8, 26.7, and 35.4°, respectively, corresponding to Fe (011, 002) (#96-230-0201), Fe<sub>2</sub>O<sub>3</sub> (024, 116) (#96-210-1168), and FeO (113) (#96-900-8637) under reaction conditions. The results provide further evidence for the Fe and Fe oxide phases under reaction conditions. When correlating these findings with performance tests, higher proportions of these reduced Fe and Fe oxide species in LR-Fe<sub>2</sub>O<sub>3</sub> and HR-Fe<sub>2</sub>O<sub>3</sub> explain their improved NH<sub>4</sub><sup>+</sup> production rates compared to pristine Fe<sub>2</sub>O<sub>3</sub>. The O 1s XPS spectra and corresponding curve fittings (Figure S11, a-c) show a clear decrease in the proportion of lattice oxygen (peak at ~ 530 eV)<sup>46</sup> after ERC, which is consistent with the reduction of Fe<sub>2</sub>O<sub>3</sub> evidenced by Fe 2p XPS spectra. Specifically, LR-Fe<sub>2</sub>O<sub>3</sub> consists of 39.7% lattice oxygen, while HR-Fe<sub>2</sub>O<sub>3</sub> comprises 34.9%, both markedly lower than pristine Fe<sub>2</sub>O<sub>3</sub> (55.8%). Two



other peaks at  $\sim 531.0$  and  $532.5$  eV are attributed to surface oxygen passivated with hydrogen and adsorbed oxygen (water), respectively.<sup>52,53</sup> The content of surface oxygen passivated with hydrogen increases from 35.4% in pristine  $\text{Fe}_2\text{O}_3$  to 43.5% in LR- $\text{Fe}_2\text{O}_3$  and further to 47.5% in HR- $\text{Fe}_2\text{O}_3$ . Similarly, adsorbed oxygen (water) increases from 8.8% in pristine  $\text{Fe}_2\text{O}_3$  to 16.8% in LR- $\text{Fe}_2\text{O}_3$  and 17.6% in HR- $\text{Fe}_2\text{O}_3$ . In fact, literature reports a direct correlation between these two oxygen species (surface oxygen passivated with hydrogen and adsorbed oxygen) and water dissociation on the catalyst surface,<sup>54–56</sup> suggesting that their elevated presence in ERC-treated samples increases water adsorption and subsequent dissociation. This process is crucial for supplying hydrogen during the  $\text{NO}_2\text{RR}$ , facilitating the hydrogenation of reaction intermediates and the eventual formation of  $\text{NH}_4^+$  production (*vide infra*).

To investigate the bulk characteristics and crystal structure of the ERC-treated catalysts at different potentials, X-ray diffraction (XRD) measurements were conducted. The XRD patterns depicted in **Figure S12** and **2b** show that pristine  $\text{Fe}_2\text{O}_3$  displays peaks at  $\sim 33.0$ ,  $35.5$ ,  $40.7$ ,  $49.4$ ,  $62.3$ , and  $63.9^\circ$ , corresponding to the (104), (110), (113), (024), (214), and (300) planes of  $\alpha\text{-Fe}_2\text{O}_3$ , respectively (JCPDS collection code: 01-080-0597). The post-conditioned electrodes, LR- $\text{Fe}_2\text{O}_3$  and HR- $\text{Fe}_2\text{O}_3$ , exhibit similar peaks, confirming the retention of the  $\alpha\text{-Fe}_2\text{O}_3$  structure. However, a new split from the (110) peak at  $\sim 35.0^\circ$ , is observed to appear in both conditioned samples (**Figure 2b, ii**). This split peak, corresponding to the (101) plane of  $\alpha\text{-Fe}_2\text{O}_3$ , indicates a partial phase shift in the crystal structure, likely caused by non-uniform distortion within the cell,<sup>57–62</sup> while the lacking of (101) peak in pristine  $\text{Fe}_2\text{O}_3$  indicates the absence of this phase shift. For samples after preconditioning reduction treatments, the  $I_{110}/I_{101}$  ratio decreases with increasing (more negative) reduction potential: HR- $\text{Fe}_2\text{O}_3$  exhibits a lower  $I_{110}/I_{101}$  of 1.47 compared to LR- $\text{Fe}_2\text{O}_3$  (1.65). This trend indicates enhanced distortion and greater phase transformation at more negative reduction treatment potentials. Such cell distortion and multiphasic phenomena have been reported in the literature as results of strong lattice strains induced in the catalysts.<sup>60,62</sup> Furthermore, previous studies have shown that the reduction of surface species (in this work,  $\text{Fe}^{3+}$  to  $\text{Fe}^{2+}/\text{Fe}$ ) can induce significant lattice strain due to localized changes in the coordination environment.<sup>63,64</sup> This strain, in turn, promotes the formation of multiphasic phenomena, as observed in XRD patterns in **Figure 2b, ii**. To confirm this, strain analysis using the Williamson-Hall (WH) equation was performed.<sup>58,65</sup> The WH plots in **Figure S13** estimate lattice strains of 6.0%, 26.3%, and 28.0% for  $\text{Fe}_2\text{O}_3$ , LR- $\text{Fe}_2\text{O}_3$ , and HR- $\text{Fe}_2\text{O}_3$ , respectively. Moreover, strain directly correlated with the d-band structure of the catalyst, modulating the adsorption energies of reaction intermediates.<sup>33,34</sup> Specifically, the increased strain can lead to the d-band center shift closer to the Fermi level,<sup>38,66,67</sup> which is responsible for the improved surface adsorption capabilities<sup>4,68–71</sup> and explains the improved water dissociation observed in HR- $\text{Fe}_2\text{O}_3$  and LR- $\text{Fe}_2\text{O}_3$  as compared to pristine  $\text{Fe}_2\text{O}_3$  as evidenced by the XPS O 1s spectra. Furthermore, the main characteristic peaks of the catalysts, corresponding to the (104), (110) and (101) planes,

were used to calculate their crystallite size (calculated via Scherrer equation) and lattice spacing, as shown in **Table S2**. The results reveal no obvious trend or significant change in crystallite size and lattice spacing with different ERC potentials. Combining XPS and XRD findings confirms that the more negative ERC potentials lead to further Fe species reduction, and thus stronger lattice strain formation, ultimately tuning the d-band center shift and leading to improved surface adsorption capabilities for protonation and  $\text{NO}_2^-$  adsorption processes. The morphology of the  $\text{Fe}_2\text{O}_3$ , LR- $\text{Fe}_2\text{O}_3$ , and HR- $\text{Fe}_2\text{O}_3$  electrodes were investigated using scanning electron (SEM) and transmission electron microscopy (TEM) (**Figure S14a** and **S14b**, respectively). The obtained SEM images of the catalysts ( $\text{Fe}_2\text{O}_3$ , LR- $\text{Fe}_2\text{O}_3$ , and HR- $\text{Fe}_2\text{O}_3$ ) were statistically analyzed to determine the particle size distribution (**Figure S15**). Specifically, the pristine  $\text{Fe}_2\text{O}_3$  catalyst displays nanoparticles (60 to 100 nm) that agglomerate into large clustered particles. After ERC, both LR- $\text{Fe}_2\text{O}_3$  and HR- $\text{Fe}_2\text{O}_3$  have a morphology consisting of a mixture of nanoparticles and flake-like aggregates, while LR- $\text{Fe}_2\text{O}_3$  shows a dominant particle size between 60 to 100 nm and HR- $\text{Fe}_2\text{O}_3$  shows a relatively smaller particle size range from 40 to 70 nm. The morphological changes are consistent with the structure distortion generated during the surface reconstruction.<sup>72,73</sup> In this study, the surface reconstruction due to lattice strain and distortion (as evidenced by the XRD measurement above) during the ECR treatment, is likely a key driver of the observed morphological changes in LR- $\text{Fe}_2\text{O}_3$  and HR- $\text{Fe}_2\text{O}_3$  electrodes. Notably, no significant change in particle size is observed, despite the catalysts being preconditioned at different reduction potentials, this is consistent with the XRD and ECSA analyses. High-resolution TEM (HR-TEM) images (**Figure 2c** and **S16**) show that all samples demonstrate lattice spacings of 0.27 and 0.25 nm corresponding to the (104) and (110) planes of  $\alpha\text{-Fe}_2\text{O}_3$ , respectively.<sup>46,48</sup> Additionally, both LR- $\text{Fe}_2\text{O}_3$  and HR- $\text{Fe}_2\text{O}_3$  display a lattice spacing of 0.26 nm, which



**Fig. 2** (a) High-resolution Fe 2p XPS spectra of  $\text{Fe}_2\text{O}_3$ , LR- $\text{Fe}_2\text{O}_3$  and HR- $\text{Fe}_2\text{O}_3$ . (b) Normalized XRD patterns (intensity normalized to the highest peak) of pristine  $\text{Fe}_2\text{O}_3$ , LR- $\text{Fe}_2\text{O}_3$ , and HR- $\text{Fe}_2\text{O}_3$ , with (i) and (ii) showing excerpts for patterns in diffraction peak range of  $30^\circ$  to  $70^\circ$  and  $32^\circ$  to  $37^\circ$ , respectively, compared with the full range ( $30^\circ$  to  $90^\circ$ ) patterns in **Figure S12**. (c) HR-TEM images of HR- $\text{Fe}_2\text{O}_3$  at (i) a magnification of 10 nm, with (ii) and (iii) showing enlarged views of specific areas indicated in (i). (d) Normalized Raman spectra of pristine  $\text{Fe}_2\text{O}_3$ , LR- $\text{Fe}_2\text{O}_3$ , and HR- $\text{Fe}_2\text{O}_3$ .



corresponds to the (101) plane of  $\alpha$ -Fe<sub>2</sub>O<sub>3</sub>, corroborating the dominant bulk  $\alpha$ -Fe<sub>2</sub>O<sub>3</sub> phase from XRD analyses.

To further understand the structure of the catalysts, Raman spectroscopy measurements were performed. The Raman spectra in **Figure 2d** for pristine Fe<sub>2</sub>O<sub>3</sub> show seven peaks at ~ 225, 244, 292, 410, 499, 612 and 661 cm<sup>-1</sup>, corresponding to  $\alpha$ -Fe<sub>2</sub>O<sub>3</sub>.<sup>74–77</sup> For both LR-Fe<sub>2</sub>O<sub>3</sub> and HR-Fe<sub>2</sub>O<sub>3</sub>, a negative shift in the  $\alpha$ -Fe<sub>2</sub>O<sub>3</sub> peaks is observed, with HR-Fe<sub>2</sub>O<sub>3</sub> exhibiting a more pronounced shift than LR-Fe<sub>2</sub>O<sub>3</sub>. This negative shift in Raman wavenumbers is likely due to changes in the electronic structure, coordination environment and/or lattice effects.<sup>78,79</sup> Thus, the more pronounced shift observed in HR-Fe<sub>2</sub>O<sub>3</sub> compared to LR-Fe<sub>2</sub>O<sub>3</sub> aligns with previous characterization results, which show higher lattice strain in HR-Fe<sub>2</sub>O<sub>3</sub> resulted from greater surface Fe species reduction. Besides, significant broadening of the Raman peaks observed in both LR-Fe<sub>2</sub>O<sub>3</sub> and HR-Fe<sub>2</sub>O<sub>3</sub> further supports the introduction of lattice strain following ERC,<sup>57</sup> consistent with XRD and HR-TEM characterization results. Hence, the observed negative shift and peak broadening in the Raman spectra of LR-Fe<sub>2</sub>O<sub>3</sub> and HR-Fe<sub>2</sub>O<sub>3</sub> can be attributed to structural disorders from non-equivalent sites in the partly reduced Fe species (Fe<sup>2+</sup>/Fe) structure and/or the built strain induced within the catalysts.<sup>57,77</sup> Nonetheless, it can be deduced that the Fe/FeO/Fe<sub>2</sub>O<sub>3</sub> components were tuned in the post-conditioned catalysts following ERC treatment. These findings collectively indicate that more negative ERC potentials lead to greater Fe<sup>3+</sup> reduction and more pronounced strain. As a result, HR-Fe<sub>2</sub>O<sub>3</sub> demonstrates the best NH<sub>4</sub><sup>+</sup> production performance from NO<sub>2</sub>RR due to its pronounced strain in the distorted structure built during the surface Fe<sub>2</sub>O<sub>3</sub> reduction.

Overall, the characterization shows that ERC creates structural disorders in the catalysts by partially reducing Fe<sub>2</sub>O<sub>3</sub> to FeO and/or metallic Fe, tuning Fe/FeO/Fe<sub>2</sub>O<sub>3</sub> components and inducing lattice strain in the catalysts. The extent of Fe<sub>2</sub>O<sub>3</sub> species reduction and strain induction increases with more negative ERC treatment potentials, with HR-Fe<sub>2</sub>O<sub>3</sub> exhibiting the most pronounced of these characteristics compared to LR-Fe<sub>2</sub>O<sub>3</sub> and pristine Fe<sub>2</sub>O<sub>3</sub>. Given that previous studies have collectively demonstrated the limited contribution of individual Fe or FeO species to enhanced NO<sub>x</sub>RR activity,<sup>30,51,80</sup> the improved NO<sub>2</sub>RR-to-NH<sub>4</sub><sup>+</sup> performance observed in this work with HR-Fe<sub>2</sub>O<sub>3</sub> and LR-Fe<sub>2</sub>O<sub>3</sub> is attributed to the synergistic effects of the tuned FeO/Fe/Fe<sub>2</sub>O<sub>3</sub> components and lattice strain. Notably, HR-Fe<sub>2</sub>O<sub>3</sub> achieves the best NO<sub>2</sub>RR activity with optimized FeO/Fe/Fe<sub>2</sub>O<sub>3</sub> components and pronounced strain, delivering the most optimal NH<sub>4</sub><sup>+</sup> production rate (154 nmol s<sup>-1</sup> cm<sup>-2</sup>) and FE<sub>NH4+</sub> (93%) at -1.0 V vs RHE.

To gain further mechanistic insight into the structural change of the active sites in the catalysts during the ERC, *in situ* Raman measurements were performed. The Raman spectra (**Figure 3a** and **3b**) reveal that the peak at ~ 408 cm<sup>-1</sup>, attributed to  $\alpha$ -Fe<sub>2</sub>O<sub>3</sub>,<sup>74–77</sup> remains until the end of the ERC treatment for all samples. However, HR-Fe<sub>2</sub>O<sub>3</sub> exhibits a greater reduction in the intensity of this peak (~ 80%) compared to LR-Fe<sub>2</sub>O<sub>3</sub> (~ 59%), indicating a more substantial reduction of Fe<sub>2</sub>O<sub>3</sub> at more negative ERC potentials. While the low signal intensity of other

$\alpha$ -Fe<sub>2</sub>O<sub>3</sub> peaks in the HR-Fe<sub>2</sub>O<sub>3</sub> spectra, likely caused by electrolyte blockage and/or high amounts of adsorbed species on the catalyst surface,<sup>81</sup> makes these peaks less visible, the predominant presence of Fe<sub>2</sub>O<sub>3</sub> in HR-Fe<sub>2</sub>O<sub>3</sub> is supported by the persistence of  $\alpha$ -Fe<sub>2</sub>O<sub>3</sub> peak at ~ 408 cm<sup>-1</sup>. Throughout the ERC, both LR-Fe<sub>2</sub>O<sub>3</sub> and HR-Fe<sub>2</sub>O<sub>3</sub> are observed to exhibit peak shifts, peak broadening, and the emergence of new shoulder peaks (marked with black arrows in the graphs), all indicative of non-uniform strain formation in the catalysts.<sup>57,79,82</sup> This non-uniform strain has been reported to significantly influence catalyst performance by altering the electronic structure and shifting the d-band center closer to the Fermi level, which is a well-recognized indicator for improving the adsorption and activation abilities of the catalysts toward reaction intermediates involved in reactions.<sup>4,33,34,68–71</sup> Comparatively, HR-Fe<sub>2</sub>O<sub>3</sub> displays these changes more prominently and earlier than LR-Fe<sub>2</sub>O<sub>3</sub>, suggesting a higher susceptibility to strain induction at more negative ERC potentials. This may explain why HR-Fe<sub>2</sub>O<sub>3</sub> exhibits the greatest NH<sub>4</sub><sup>+</sup> production performance from NO<sub>2</sub>RR. Unlike *ex situ* Raman and XPS analyses, *in situ* Raman spectra do not consistently show a negative shift to lower wavenumbers or the FeO peak at approximately 580 cm<sup>-1</sup>. This discrepancy suggests that the FeO observed in *ex situ* analyses may not be attributed to the residual oxide after surface reduction, which is possibly attributed to the reconstructed FeO during the reoxidation when exposed to air after the reaction.<sup>83</sup> Thus, *in situ* Raman provides a clear view of the structural changes occurring within the catalysts at different ERC potentials. These results demonstrate that HR-Fe<sub>2</sub>O<sub>3</sub>, preconditioned at a more negative ERC potential, possesses more structural disorders through more obvious reduction of Fe<sub>2</sub>O<sub>3</sub> into Fe<sup>2+</sup>/Fe species while building lattice strain, collectively leading to enhanced NH<sub>4</sub><sup>+</sup> production performance from NO<sub>2</sub>RR.

Further, *in situ* Fourier transform infrared (FTIR) spectroscopy measurements were conducted under electrochemical NO<sub>2</sub>RR conditions with electrolyte (0.1 M KOH + 0.1 M KNO<sub>2</sub>) at -1.0 V vs RHE for 15 min to probe the reaction intermediate species and elucidate the reaction pathways undertaken by these catalysts for producing NH<sub>4</sub><sup>+</sup>. The *in situ* FTIR spectra, shown in **Figure 3c** and **S17**, reveal peaks corresponding to various intermediates, i.e., NH<sub>2</sub>OH\* (1215 cm<sup>-1</sup>), NO<sub>2</sub>\* (1362 cm<sup>-1</sup>), NH<sub>2</sub>\* (1563 cm<sup>-1</sup>), NH<sub>3</sub>\* (1767 cm<sup>-1</sup>), NO\* (1971 cm<sup>-1</sup>), NH<sub>4</sub>\* (3142 cm<sup>-1</sup>), and H<sub>2</sub>O\* (3500 cm<sup>-1</sup>).<sup>44,84–92</sup> Therefore, in agreement with the literature,<sup>3,6,8,44</sup> this *in situ* FTIR measurement validates the reaction mechanism for the eR-Fe<sub>2</sub>O<sub>3</sub> catalysts. Specifically, the ionic NO<sub>2</sub><sup>-</sup> is adsorbed onto the catalyst surface to form NO<sub>2</sub>\*, the N-O bond of which then cleave to form NO\*. The formed NO\* is hydrogenated subsequently to produce HNO\*, H<sub>2</sub>NO\*, NH<sub>2</sub>OH\*, NH<sub>2</sub>\*, NH<sub>3</sub>\*, NH<sub>4</sub>\*, which ultimately desorbed to form NH<sub>4</sub><sup>+</sup>. Moreover, it is observed that both NO<sub>2</sub>\* and NO\* peaks (at ~ 1362 and 1971 cm<sup>-1</sup>, respectively) exhibit a production trend in pristine Fe<sub>2</sub>O<sub>3</sub>, but a consumption trend in LR-Fe<sub>2</sub>O<sub>3</sub> and HR-Fe<sub>2</sub>O<sub>3</sub>, suggesting enhanced conversion of these intermediates over the post-conditioned catalysts. When comparing LR-Fe<sub>2</sub>O<sub>3</sub> and HR-Fe<sub>2</sub>O<sub>3</sub>, HR-Fe<sub>2</sub>O<sub>3</sub> shows boosted consumption rate of NO\* and NO<sub>2</sub>\*



during the *in situ* experiment, benefiting from the structure reconstruction under the more negative ERC treatment potential as discussed above. Additionally, all samples display a production trend for  $\text{NH}_2\text{OH}^*$ ,  $\text{NH}_2^*$ ,  $\text{NH}_3^*$ , and  $\text{NH}_4^*$  peaks. Notably, the HR- $\text{Fe}_2\text{O}_3$  demonstrated the most significant increase in  $\text{NH}_2\text{OH}^*$  peak (at  $\sim 1215\text{ cm}^{-1}$ ) intensity compared to pristine  $\text{Fe}_2\text{O}_3$  and LR- $\text{Fe}_2\text{O}_3$ . These results collectively suggest that ERC treatment promotes effective adsorption and faster consumption of  $\text{NO}_2\text{RR}$  intermediates ( $\text{NO}_2^*$  and  $\text{NO}^*$ ), leading to improved hydrogenation pathways and ultimately higher  $\text{NH}_4^+$  productivity. This demonstrates that the effects of ERC-induced structural disorders, i.e., optimized  $\text{Fe}^{3+}/\text{Fe}^{2+}/\text{Fe}$  components and lattice strain, collectively drive superior  $\text{NO}_2\text{RR}$ -to- $\text{NH}_4^+$  performance.

To gain insight into the enhanced  $\text{NO}_2\text{RR}$  performance, density functional theory (DFT) calculations were performed on pristine and defective hematite ( $\alpha\text{-Fe}_2\text{O}_3$ ) (104) surfaces. The (104) surface was selected as it represents the most prominent surface orientation in pristine hematite before ERC. Given that ERC reduces the surface oxide and introduced structural disorders, the (104) surface with oxygen vacancies was investigated to study the defective surface effects on  $\text{NO}_2^-$  adsorption and water activation processes. The calculations reveal that  $\text{NO}_2^-$  exhibits stronger adsorption on the coordinatively unsaturated Fe site adjacent to the vacancy (-

on pristine surfaces (-1.25 eV) to a tilted configuration with hydrogen atoms oriented closer to the surface on vacancy slab (-1.55 eV), facilitating water dissociation and creating a favorable environment for proton-coupled electron transfer processes (**Figure S20**). This enhanced water activation capability ensures a steady supply of surface protons ( $\text{H}^*$ ) required for the improved hydrogenation steps observed in the FTIR measurements, providing molecular-level understanding of why ERC treatment enhances  $\text{NO}_2\text{RR}$  performance.

Further,  $\text{NO}_2\text{RR}$  performance of all samples ( $\text{Fe}_2\text{O}_3$ , LR- $\text{Fe}_2\text{O}_3$ , and HR- $\text{Fe}_2\text{O}_3$ ) was evaluated over extended periods through a 15-cycle test at -1.0 V vs RHE, with each cycle comprising 0.5 h of chronoamperometry. Cycling tests were selected over continuous long-term testing to mitigate issues related to electrolyte depletion and concentration drift over time, which occur due to the consumption and gradual depletion of  $\text{NO}_2^-$  species in a batch mode setup.<sup>8,93,94</sup> By mimicking this through cycling test, it ensures reproducible stability evaluation and a more reliable assessment of catalyst performance under conditions closer to practical operation. As evidenced by the steady chronoamperometric *i-t* curves and stable  $\text{NH}_4^+$  production rate shown in **Figure S18**, all electrodes demonstrate high  $\text{NO}_2\text{RR}$  activity over prolonged periods, confirming their stability. Among them, HR- $\text{Fe}_2\text{O}_3$  catalyst exhibits the highest  $\text{NO}_2\text{RR}$  performance, achieving an average  $\text{NH}_4^+$  production rate of  $153.0\text{ nmol s}^{-1}\text{ cm}^{-2}$  and  $\text{FE}_{\text{NH}_4^+}$  of 93%, which is competitive with findings reported in the literature (**Table S3**). While  $\text{NH}_4^+$  production rate and  $\text{FE}_{\text{NH}_4^+}$  are critical metrics for evaluating catalyst performance, the HR- $\text{Fe}_2\text{O}_3$  catalyst also excels in other key performance metrics.<sup>89</sup> Specifically, it demonstrates an exceptionally high partial current density for  $\text{NH}_4^+$  production, reaching  $\sim 96.5\text{ mA cm}^{-2}$  at -1.0 V vs RHE, positioning it among the most active  $\text{NO}_2\text{RR}$  catalyst for  $\text{NH}_4^+$  generation in literature (**Table S3**). While it is also important to evaluate  $\text{NO}_2\text{RR}$  performance at lower concentrations and in conditions representative of real wastewater ( $\text{NO}_x$  concentration ranging from 0.88 mM to 1.95 M),<sup>99,100</sup> the investigation extends to experiment with PAE (plasma air activated electrolyte). This electrolyte solution is generated using a plasma system as discussed in previous works<sup>6,44,81</sup> (**Experimental Section**). Through this approach, it enables a decentralized, air-to-ammonia production pathway, independent of wastewater sources, thus broadening its applicability across a wide range of deployable scenarios. Building on previous studies, this work focuses on optimizing the production of  $\text{NO}_2^-$  over  $\text{NO}_3^-$  by manipulating various operating conditions. First, the pH of the reaction medium solution was altered: comparing neutral (deionized water) to alkaline conditions (0.1 M KOH). The results (**Figure S19a**) indicate that the alkaline condition (0.1 M KOH) significantly favors the production of  $\text{NO}_2^-$  (9.6 mM) over  $\text{NO}_3^-$  (0.8 mM), whereas in neutral environments, the production trends reverse, favoring  $\text{NO}_3^-$  over  $\text{NO}_2^-$ . Further, the production of  $\text{NO}_x$  via plasma was tested across different plasma voltages, as voltage is reported to fundamentally affect the concentration of  $\text{NO}_x$  production.<sup>101,102</sup> The results (**Figure S19b**) indicate that the highest amounts of  $\text{NO}_2^-$  and total  $\text{NO}_x$  are produced at 200 V,

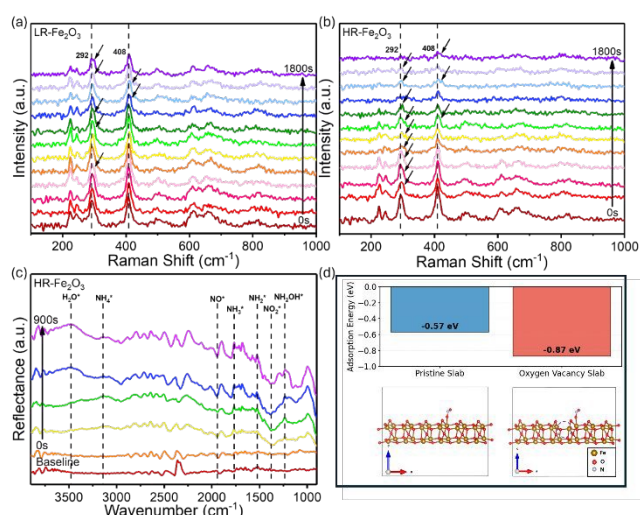


**Fig. 3** *In situ* Raman spectra of (a) LR- $\text{Fe}_2\text{O}_3$  and (b) HR- $\text{Fe}_2\text{O}_3$  during 30-min ERC treatment in electrolyte condition of 0.1 M KOH + 0.1 M  $\text{KNO}_2$ . Black arrows mark the emergence of peak broadening and new shoulder peaks. (c) *In situ* FTIR spectra of HR- $\text{Fe}_2\text{O}_3$  at  $\text{NO}_2\text{RR}$  applied potential of -1.0 V vs RHE for 15 mins in electrolyte condition of 0.1 M KOH + 0.1 M  $\text{KNO}_2$ . (d) DFT calculations of  $\text{NO}_2^-$  adsorption energy on simulated surface representing pristine (pristine slab) and defective (oxygen vacancy slab) hematite ( $\alpha\text{-Fe}_2\text{O}_3$ ) (104) surfaces.

0.87 eV) compared to the pristine surface (-0.57 eV) (**Figure 3d**). This correlates with the experimentally observed enhanced  $\text{NO}_2^-$  conversion rates in ERC-treated catalysts. Along with enhanced nitrite binding, oxygen vacancies act as bifunctional active sites that fundamentally alter water interactions. While water dissociation on the pristine surface is thermoneutral (-0.04 eV), vacancy formation renders this process exothermic (-0.21 eV). The preferred water binding mode shifts from O-down



with concentrations of 13.7 and 15.0 mM, respectively. NO<sub>x</sub>RR performance testing in the optimally produced PAAE was conducted for 10 cycles (0.5 h chronoamperometry each cycle) within a commercial H-cell using pristine Fe<sub>2</sub>O<sub>3</sub> and the best performing catalyst, HR-Fe<sub>2</sub>O<sub>3</sub>. The results further demonstrate the high stability of both Fe<sub>2</sub>O<sub>3</sub> and HR-Fe<sub>2</sub>O<sub>3</sub> across the 10-cycle operation at -1.0 V vs RHE, evidenced by steady chronoamperometric *i-t* curves and consistent NH<sub>4</sub><sup>+</sup> production rates (Figure S20a and S20b, respectively). Additionally, the results suggest that HR-Fe<sub>2</sub>O<sub>3</sub> outperforms pristine Fe<sub>2</sub>O<sub>3</sub> even under low NO<sub>x</sub> concentrations, achieving a stable NH<sub>4</sub><sup>+</sup> production rate of 32.0 nmol s<sup>-1</sup> cm<sup>-2</sup> and a steady current density of ~ 52 mA cm<sup>-2</sup> across 10-cycle tests at -1.0 V vs RHE. These results are comparable to those reported in the literature (Table S3) for studies involving similar low concentrations of NO<sub>x</sub>. Hence, conducting NO<sub>x</sub>RR using PAAE reveals the potential for a self-sustaining NH<sub>4</sub><sup>+</sup> production system through the integration of a plasma-electrolyzer setup. Furthermore, the ability of HR-Fe<sub>2</sub>O<sub>3</sub> to efficiently convert trace amounts of NO<sub>x</sub> to NH<sub>4</sub><sup>+</sup> in PAAE underscores its potential for real-world applications, particularly in treating waste streams from industries, power plants, and agriculture where NO<sub>x</sub> is commonly found at low concentrations.

### 3 Conclusions

In conclusion, this work addresses the key knowledge gaps regarding the ERC-treated Fe-based catalysts with structural disorders in enhancing NO<sub>2</sub>RR activity for NH<sub>4</sub><sup>+</sup> production in alkaline environments. A combination of *ex situ* and *in situ* characterization techniques collectively reveals that more negative ERC potentials enhance the reduction of surface Fe<sub>2</sub>O<sub>3</sub> to FeO and metallic Fe, optimizing Fe<sup>3+</sup>/Fe<sup>2+</sup>/Fe components, while simultaneously inducing significant lattice strain. This strain alters the d-band structure, promoting the hydrogenation of NO<sub>2</sub>RR intermediates and enhancing NH<sub>4</sub><sup>+</sup> production. These findings underscore the synergistic effects of lattice strain engineering and Fe<sup>3+</sup>/Fe<sup>2+</sup>/Fe components in creating highly effective active sites for NO<sub>2</sub>RR, offering valuable insights for designing next-generation metal oxide catalysts. Additionally, this work addresses significant knowledge gaps in utilizing plasma technology to optimize NO<sub>x</sub> feedstocks generation for NO<sub>2</sub><sup>-</sup> formation. Systematic optimization of plasma conditions (solution pH and reactor voltage) enhances NO<sub>2</sub><sup>-</sup> generation up to 13.7 mM, thereby offering a more efficient and targeted feedstock for NO<sub>2</sub>RR. Overall, this work showcases the direct reduction of NO<sub>2</sub><sup>-</sup> to NH<sub>4</sub><sup>+</sup> offers substantial advantages for green ammonia production, bypassing the most energy-intensive NO<sub>3</sub><sup>-</sup>-to-NO<sub>2</sub><sup>-</sup> step and reducing overall energy costs. The enhanced hydrogenation capabilities of structurally engineered Fe<sub>2</sub>O<sub>3</sub> catalysts in this work enables greater selectivity toward NH<sub>4</sub><sup>+</sup>, with minimal H<sub>2</sub> by-products, thereby improving sustainability. Moreover, the integration of this plasma-electrolyzer system enables a decentralized, self-sustaining pathway for transforming air-derived NO<sub>x</sub> into ammonia-related products on demand.

## 4 Experimental

### 4.1 Materials

All chemical reagents and solvents utilized in this work were used as received and without any further purification. Deionized water (resistivity 18.2 MΩ cm<sup>-1</sup>) was used throughout all experiments.

### 4.2 Catalyst Synthesis

Fe<sub>2</sub>O<sub>3</sub> catalyst powders were prepared through a precipitation method followed by calcination. First, 2 g of iron (III) nitrate nonahydrate (Sigma Aldrich, ≥ 99.95 %) was dissolved in 15 mL of deionized water and stirred for 0.5 h to achieve a homogeneous solution. This solution was then gradually added dropwise to 100 mL of a 1 mol L<sup>-1</sup> Na<sub>2</sub>CO<sub>3</sub> (Chem-Supply, analytical grade, 99.5 %) solution maintained at 60 °C. The mixture was aged and stirred continuously for 3 h. The resulting slurry was centrifuged and washed with ethanol (Chem-Supply, analytical grade, 99.5 %) and water (3 to 5 times each) to remove impurities, then dried overnight at 100 °C. The black crystals obtained were ground into powders and calcined in flowing air (Coregas, purity 100%) at 400 °C for 2 h, yielding brown Fe<sub>2</sub>O<sub>3</sub> powders.

To prepare pristine Fe<sub>2</sub>O<sub>3</sub> working electrodes, these Fe<sub>2</sub>O<sub>3</sub> powders were spray-cast onto carbon fibre paper. Specifically, 3 mg of Fe<sub>2</sub>O<sub>3</sub> powder was dispersed in a solution containing 1 mL deionized water, 1 mL ethanol, and 30 μL of a Nafion 117 solution (Sigma-Aldrich, ~ 5% in a mixture of lower aliphatic alcohols and water). The mixture was sonicated for 10 to 15 mins to ensure homogeneity. One-third of this mixture was sprayed onto carbon fibre paper placed on a hot plate at 110 °C, evenly covering an area of 1 cm × 6 cm. After cooling, the sprayed carbon fibre paper was cut into six pristine Fe<sub>2</sub>O<sub>3</sub> electrodes.

To modify the surface properties of Fe<sub>2</sub>O<sub>3</sub>, ERC strategy was employed, with the ERC treated Fe<sub>2</sub>O<sub>3</sub> electrodes referred to as eR-Fe<sub>2</sub>O<sub>3</sub>. Specifically, prior to electrochemical testing, the Fe<sub>2</sub>O<sub>3</sub> electrodes were pre-treated at reduction potentials of -1.0 V and -2.0 V vs RHE for 0.5 h. The Fe<sub>2</sub>O<sub>3</sub> electrodes conditioned at -1.0 V are referred to as Low-Reduction Fe<sub>2</sub>O<sub>3</sub> (LR-Fe<sub>2</sub>O<sub>3</sub>), while those treated at -2.0 V are named as High-Reduction Fe<sub>2</sub>O<sub>3</sub> (HR-Fe<sub>2</sub>O<sub>3</sub>). This pre-treatment was conducted in a commercial three-electrode H-cell containing 0.1 M KOH (Sigma Aldrich, ACS reagent grade, 90 % flakes) and 0.1 M KNO<sub>2</sub> (Sigma Aldrich, ACS reagent grade, ≥ 96.0 %) as the catholyte, similar to the setup used for electrochemical NO<sub>2</sub>RR-to-NH<sub>4</sub><sup>+</sup> activity testing.

### 4.3 Electrochemical Experiments

All chemical reagents and solvents utilized in this work were used as received and without any further purification. Deionized water (resistivity 18.2 MΩ cm<sup>-1</sup>) was used throughout all experiments. The electrocatalytic NO<sub>2</sub>RR-to-NH<sub>4</sub><sup>+</sup> was carried out using a commercial H-cell setup. A three-electrode system was employed, comprising the eR-Fe<sub>2</sub>O<sub>3</sub> catalyst as the working electrode (cathode), a Pt plate as the counter electrode (anode), and a Hg/HgO reference electrodes. The anolyte was 50 mL of 0.1 M KOH solution, whereas the catholyte was 50 mL



of 0.1 M KOH with 0.1 M KNO<sub>2</sub>. An anion exchange membrane (AEM) (Dioxide Materials, X37-50 Grade RT) was used to separate the electrolytes while allowing ions to pass through. PAAE was also used as catholyte to evaluate the NO<sub>2</sub>RR performance of the catalysts at lower concentrations and in conditions representative of real wastewater.<sup>99,100</sup> All electrochemical NO<sub>2</sub>RR processes were performed using an Autolab Potentiostat (Nova 2 Metrohm).

Chronoamperometry tests were employed to identify the optimal potential for maximum NH<sub>4</sub><sup>+</sup> production efficiency. Each test was conducted for a duration of 15 mins and repeated three times to obtain average values. All potentials were converted to the RHE using the following equations:<sup>103–105</sup>

$$E_{RHE} (V) = E_{Hg/HgO} (V) + 0.098 + 0.059 \times pH$$

Long-term stability was assessed at the optimal applied potential under conditions similar to the chronoamperometry tests. The stability tests consisted of 15 cycles at the optimal potential, with each cycle lasting 30 mins. LSV measurements were conducted using the same H-cell setup under three different catholyte conditions: 0.1 M KOH, 0.1 M KOH + 0.1 M KNO<sub>3</sub>, and 0.1 M KOH + 0.1 M KNO<sub>2</sub>. EIS experiments were performed under similar conditions to the chronoamperometry tests, with a frequency range from 1 MHz to 0.01 Hz. The measurements were taken at potential of 0.615 V vs RHE.

The ECSAs of the catalysts were estimated using the CDL method. Briefly, cyclic voltammetry (CV) scans were recorded within a potential window of  $\pm 0.05$  V around each catalyst's onset potential, as identified from the LSV curves. The scan rates used were 100, 200, 300, 400, and 500 mV s<sup>-1</sup>. The differences between the cathodic and anodic currents at the midpoint potential were plotted against the scan rates. The slope of the linear fit to this plot corresponds to the CDL. The ECSA was then calculated by dividing the CDL of the catalyst by the specific capacitance of a reference blank glassy carbon electrode (40  $\mu$ F cm<sup>-2</sup>) and multiplying by the geometric surface area of the electrode.<sup>45</sup>

#### 4.4 Products Analysis

The main text of the article should appear here with headings as appropriate. The concentration of NH<sub>4</sub><sup>+</sup> produced in the catholyte was determined using the indophenol blue test. In this method, 0.5 mL of the catholyte sample was transferred into a 1.5 mL sample tube. To this, 0.4 mL of a 1 M NaOH solution (Sigma-Aldrich semiconductor grade, 99.99%) containing 5 wt.% salicylic acid (Sigma-Aldrich ACS grade, 99.0%) and 5 wt.% sodium citrate (Sigma-Aldrich ACS grade, 99.0%) was added, followed by 0.1 mL of a 0.05 M sodium hypochlorite solution (Sigma-Aldrich ACS grade, 10–15%) and 30  $\mu$ L of a 1 wt.% sodium nitroferricyanide solution (Sigma-Aldrich ACS grade, 99 %). The mixture was thoroughly mixed and incubated in the dark at room temperature for 1 h. If the NH<sub>4</sub><sup>+</sup> concentration was excessively high, the catholyte was appropriately diluted prior to analysis. After incubation, the amount of NH<sub>4</sub><sup>+</sup> was quantified using ultraviolet-visible (UV-Vis) spectroscopy (Shimadzu, UV-360). Absorbance measurements were taken over wavelengths ranging from 550 to 800 nm. A calibration curve was constructed using the peak absorbance

values (Figure S21). The performance of the catalysts in generating NH<sub>4</sub><sup>+</sup> was assessed by calculating the production rate (Rate<sub>NH<sub>4</sub><sup>+</sup></sub>) and Faradaic efficiency (FE<sub>NH<sub>4</sub><sup>+</sup></sub>) using the following equations:<sup>106,107</sup>

$$\text{Rate}_{\text{NH}_4^+} = \frac{[\text{NH}_4^+] \cdot V}{t \cdot S}$$

$$\text{FE}_{\text{NH}_4^+} = \frac{n \cdot F \cdot [\text{NH}_4^+] \cdot V}{Q}$$

where  $V$  is the volume of catholyte,  $t$  is time taken for NO<sub>2</sub>RR,  $S$  is the effective area of working electrode,  $n$  is the desired electrons to synthesis one NH<sub>4</sub><sup>+</sup> molecule ( $n = 6$ ),  $F$  is the Faraday constant ( $F = 96485.33$  As mol<sup>-1</sup>) and  $Q$  is the overall electrical energy consumed by electrodes throughout the duration of the electrochemical NO<sub>2</sub>RR process.

In addition, ion chromatography (IC) was employed to quantify the concentrations of NH<sub>4</sub><sup>+</sup>, NO<sub>2</sub><sup>-</sup>, and NO<sub>3</sub><sup>-</sup> and validate the calorimetric methods. The analyses were performed using an AQ400 ion chromatograph from Seal Analytical. To measure the amount of H<sub>2</sub> produced in the cathodic chamber, the solution was purged with Ar (Coregas, > 99.95% purity) gas for approximately 15 mins before conducting performance tests. A Shimadzu GC-2010 gas chromatography (GC) equipped with a thermal conductivity detector (TCD) and a Supelco Carboxen 1010 column was used for analysis. A calibration curve (Figure S22) was generated using known concentrations of H<sub>2</sub> to ensure accurate quantification.

#### 4.5 Physical Characterization

For the study of surface morphology, crystal size, and surface element distribution of the catalysts, a Nano SEM 230 scanning electron microscope (SEM) and a FEI Tecnai G2 20 transmission electron microscope (TEM) were utilized. An accelerating voltage of 200 kV was applied for the TEM measurement. To prepare samples for TEM analysis, the catalyst nanoparticles were first scrapped off from the electrode substrate. They were then dispersed in ethanol by gentle ultrasonic agitation for a few minutes. Using a micropipette, a small droplet of the resulting dispersed suspension was drop-cast onto a gold TEM grid. Finally, the samples were dried under ambient conditions before being used for TEM measurement. X-ray diffraction (XRD) studies were performed using a XPERTPRO diffractometer with Cu K $\alpha$  radiation ( $\lambda = 1.54060$  Å). The scanning range spanned from 10° to 90° with a step size of 0.013°, aiming to identify the phase compositions and crystallinity of the catalysts. Data collected from the XRD experiments were analyzed using the Highscore Plus software.

The surface chemical states of the catalysts were investigated using a Thermo ESCALAB250Xi X-ray photoelectron spectrometer (XPS). A monochromatic Al K $\alpha$  source with an excitation energy of 1486.68 eV was employed. The instrument operated at a typical power of 120 W, with an average spot size of 500  $\mu$ m in diameter. Survey scans were recorded with a pass energy of 100 eV. While detailed regional scans used a pass energy of 20 eV. Calibration of the C 1s XPS spectra were performed by setting the graphitic C-C peak position to 284.8 eV. Raman spectra were acquired at room temperature using either an inVia 2 or an inVia Qontor Raman spectrometer. The inVia 2 instrument utilized a 532 nm wavelength diode laser



with 50 × magnification, while the inVia Qontor used a 514 nm diode laser, also at 50 × magnification. These measurements provided insights into the surface chemistry and composition of the catalysts. Additionally, *in situ* Raman measurements were conducted under applied potentials corresponding to the electrochemical reactions being studied, maintaining similar operational parameters.

*In situ* Fourier transform infrared (FTIR) measurements were performed at the infrared beamline of the Australian Synchrotron. The experimental setup involved a three-electrode electrochemical cell equipped with a ZnSe crystal serving as the infrared transmission window. An Ag/AgCl electrode acted as the reference electrode, while a Pt wire served as the counter electrode. The working electrode (i.e., pristine Fe<sub>2</sub>O<sub>3</sub>, LR-Fe<sub>2</sub>O<sub>3</sub>, and HR-Fe<sub>2</sub>O<sub>3</sub>) was connected to a potentiostat to apply the required potential for the electrochemical reaction under investigation. FTIR spectra were continuously collected during the experiments in reflection mode at a resolution of 4 cm<sup>-1</sup>. To enhance the signal-to-noise ratio, each spectrum was the result of accumulating 512 scans. Background spectra were obtained using the same setup at open-circuit voltage before commencing the tests.

*In situ* Fe K-edge XANES measurement was carried out at the XAS beamline of the Australian Synchrotron Center. The Data were collected in fluorescence mode using a solid-state 18-element detector. The *in situ* cell was mounted on the beamline sample stage, with the electrode oriented at a 45° angle relative to the fluorescence detector.<sup>108</sup> The incident beam intensity was monitored using an OKEN ionization chamber, and all measurements were performed at ambient temperature.

*In situ* powder diffraction (PD) experiments were carried out using a custom-designed three-electrode electrochemical cell, equipped with a Kapton window (2 cm diameter) to enable X-ray irradiation.<sup>109</sup> For the measurements, the cell was configured with an Ag/AgCl electrode as the reference, a Pt wire as the counter electrode, and the prepared catalyst as the working electrode.

#### 4.6 Plasma System for PAAE Generation

An in-house, custom-built plasma system (as described in the work by Jing et al.<sup>6</sup>), comprising of a plasma generator ('Leap 100' from PlasmaLeap Technologies) and a plasma reactor generating PAAE (plasma air activated electrolyte), was set up as illustrated in **Figure S23**. The plasma reactor was filled with 250 mL of 0.1 M KOH. Air (Coregas, purity 100%) was fed into the plasma system at a constant flowrate of 20 L/min. The plasma system reaction was operated under constant plasma generator operating parameters (i.e., voltage, duty, discharge frequency, and resonance frequency) for 2 h, with the solution in the reactor continuously stirred at constant speed of 350 rpm. After 2 h, the plasma activated solution, PAAE rich in NO<sub>x</sub> species, including NO<sub>2</sub><sup>-</sup> and NO<sub>3</sub><sup>-</sup>, was cooled down to room temperature before being used for subsequent electrochemical measurements.

#### 4.7 Computational Methods

All spin-polarized calculations were implemented using the Vienna Ab initio Simulation Package (VASP) with the Projector

Augmented Wave (PAW) method, interfaced through the Atomic Simulation Environment (ASE).<sup>110</sup> Electronic wavefunctions were expanded in a plane wave basis set with a 500 eV cutoff energy using gamma-point calculations. Electronic self-consistency was achieved with a convergence criterion of 10<sup>-6</sup> eV, while ionic relaxations were terminated when forces on all unconstrained atoms fell below 0.05 eV/Å. The Perdew-Burke-Ernzerhof (PBE) functional was employed to account for exchange-correlation effects within the generalized gradient approximation (GGA) framework. To accurately account for the strongly correlated Fe 3d electrons, the DFT+U approach was implemented with a Hubbard U parameter of 4.2 eV for Fe atoms, following the Dudarev's formalism. To model hematite surfaces a five-layer α-Fe<sub>2</sub>O<sub>3</sub>(104) slab with a 15 Å vacuum gap in the z-direction was constructed (**Figure S24**). The top three atomic layers were fully relaxed to interact with adsorbates, while the bottom two layers were constrained to maintain bulk-like properties. The charged NO<sub>2</sub><sup>-</sup> species was avoided as a reference in our DFT calculation. A thermodynamic cycle method was instead used to find the reference energy for NO<sub>2</sub><sup>-</sup>. This approach uses the deprotonation of HNO<sub>2</sub> as a reference.

#### Conflicts of interest

There are no conflicts to declare.

#### Data availability

The data supporting this article have been included as part of the supplementary information (SI). Supplementary Information is available. See DOI: <https://doi.org/xxx>.

#### Acknowledgements

The work was supported by the Australian Research Council (ARC) Training Centre for Global Hydrogen Economy (IC200100023). The authors acknowledge research funding provided by the ARC (DE230100789 and DE230101396). R.D. acknowledges funding from UNSW Scientia Fellowship. Z. M. acknowledges UNSW-Tsinghua Collaborative Research Seed Program 2023 and the fellowship program by the International Hydrogen Research Collaboration Program funded by Commonwealth Scientific and Industrial Research Organisation (CSIRO). The authors also acknowledge the Infrared Microscopy/ANSTO Grant (AS241/IRM/21262) for the *in situ* FTIR beamtime, XAS/ANSTO Grant (AS261/XAS/24311a) for the *in situ/ ex situ* XANES, and PD/ANSTO Grant at the Australian Synchrotron

#### References

- 1 Eliseev, G. In *2024 Annual Conference (Fertecon/S&P Global Commodity Insights)*; S&P Global Commodity Insights (Fertecon): Conference Presentation, 2024; pp 1–17.
- 2 Wang, H.; Lin, N.; Arzumanyan, M. *Gases* **2024**, *4*, 224–235. <https://doi.org/10.3390/gases4030013>.



- 3 Wang, Y.; Zhou, W.; Jia, R.; Yu, Y.; Zhang, B. *Angew. Chemie Int. Ed.* **2020**, *59* (13), 5350–5354. <https://doi.org/10.1002/anie.201915992>.
- 4 Wang, Y.; Xu, A.; Wang, Z.; Huang, L.; Li, J.; Li, F.; Wicks, J.; Luo, M.; Nam, D.-H.; Tan, C.-S.; Ding, Y.; Wu, J.; Lum, Y.; Dinh, C.-T.; Sinton, D.; Zheng, G.; Sargent, E. H. *J. Am. Chem. Soc.* **2020**, *142* (12), 5702–5708. <https://doi.org/10.1021/jacs.9b13347>.
- 5 Guo, Y.; Zhang, R.; Zhang, S.; Zhao, Y.; Yang, Q.; Huang, Z.; Dong, B.; Zhi, C. *Energy Environ. Sci.* **2021**, *14* (7), 3938–3944. <https://doi.org/10.1039/d1ee00806d>.
- 6 Sun, J.; Alam, D.; Daiyan, R.; Masood, H.; Zhang, T.; Zhou, R.; Cullen, P. J.; Lovell, E. C.; Jalili, A.; Amal, R. *Energy Environ. Sci.* **2021**, *14* (2), 865–872. <https://doi.org/10.1039/d0ee03769a>.
- 7 Serpell, O.; Hsain, Z.; Chu, A.; Johnsen, W. *Ammonia's Role in a Net-Zero Hydrogen Economy*; 2023.
- 8 Daiyan, R.; Tran-Phu, T.; Kumar, P.; Iputera, K.; Tong, Z.; Leverett, J.; Khan, M. H. A.; Asghar Esmailpour, A.; Jalili, A.; Lim, M.; Tricoli, A.; Liu, R.-S.; Lu, X.; Lovell, E.; Amal, R. *Energy Environ. Sci.* **2021**, *14* (6), 3588–3598. <https://doi.org/10.1039/d1ee00594d>.
- 9 Smith, C.; Hill, A. K.; Torrente-Murciano, L. *Energy Environ. Sci.* **2020**, *13* (2), 331–344. <https://doi.org/10.1039/c9ee02873k>.
- 10 Ye, D.; Tsang, S. C. E. *Nat. Synth.* **2023**, *2* (7), 612–623. <https://doi.org/10.1038/s44160-023-00321-7>.
- 11 Carreon, M. L. *J. Phys. D. Appl. Phys.* **2019**, *52* (48), 483001. <https://doi.org/10.1088/1361-6463/ab3b2c>.
- 12 Bian, X.; Zhao, Y.; Zhang, S.; Li, D.; Shi, R.; Zhou, C.; Wu, L. Z.; Zhang, T. *ACS Mater. Lett.* **2021**, *3* (11), 1521–1527. [https://doi.org/10.1021/ACSMATERIALSLETT.1C00504/SUPPL\\_FILE/TZ1C00504\\_SI\\_001.PDF](https://doi.org/10.1021/ACSMATERIALSLETT.1C00504/SUPPL_FILE/TZ1C00504_SI_001.PDF).
- 13 Lin, B.; Wiesner, T.; Malmali, M. *ACS Sustain. Chem. Eng.* **2020**, *8* (41), 15517–15531. <https://doi.org/10.1021/acssuschemeng.0c04313>.
- 14 Hawtof, R.; Ghosh, S.; Guarr, E.; Xu, C.; Sankaran, R. M.; Renner, J. N. *Asian J. Chem.* **2019**, *31* (2), 5778–5789. <https://doi.org/10.1126/sciadv.aat5778>.
- 15 He, Y.; Chen, Z.; Li, Z.; Niu, G.; Tang, J. *Front. Optoelectron.* **2018**, *11* (1), 92–96. <https://doi.org/10.1007/s12200-018-0807-z>.
- 16 Giddey, S.; Badwal, S. P. S.; Munnings, C.; Dolan, M. *ACS Sustain. Chem. Eng.* **2017**, *5* (11), 10231–10239. <https://doi.org/10.1021/acssuschemeng.7b02219>.
- 17 Kumari, S.; Pishgar, S.; Schwarting, M. E.; Paxton, W. F.; Spurgeon, J. M. *Chem. Commun.* **2018**, *54* (95), 13347–13350. <https://doi.org/10.1039/c8cc07869f>.
- 18 Du, H. L.; Chatti, M.; Hodgetts, R. Y.; Cherepanov, P. V.; Nguyen, C. K.; Matuszek, K.; MacFarlane, D. R.; Simonov, A. N. *Nature* **2022**, *609* (7928), 722–727. <https://doi.org/10.1038/s41586-022-05108-y>.
- 19 Chen, H.; Yuan, D.; Wu, A.; Lin, X.; Li, X. *Waste Dispos. Sustain. Energy* **2021**, *3*, 201–217. <https://doi.org/10.1007/s42768-021-00074-z>.
- 20 Li, L.; Tang, C.; Cui, X.; Zheng, Y.; Wang, X.; Xu, H.; Zhang, S.; Shao, T.; Davey, K.; Qiao, S.-Z. *Angew. Chemie* **2021**, *133* (25), 14250–14256. <https://doi.org/10.1002/anie.202104394>.
- 21 Li, W.; Zhang, S.; Ding, J.; Liu, J.; Wang, Z.; Zhang, H.; Ding, J.; Chen, L.; Liang, C. *ACS Sustain. Chem. Eng.* **2023**, *11* (3), 1168–1177. <https://doi.org/10.1021/acssuschemeng.2c06525>.
- 22 Zhang, Z.; Zhang, N.; Zhang, J.; Deng, B.; Cao, Z.; Wang, Z.; Wei, G.; Zhang, Q.; Jia, R.; Xiang, P.; Xia, S. *Chem. Eng. J.* **2024**, *483*, 148952. <https://doi.org/10.1016/j.cej.2024.148952>.
- 23 Yin, S.; Cao, R.; Han, Y.; Shang, J.; Zhang, J.; Jiang, W.; Liu, G. *J. Energy Chem.* **2024**, *96*, 642–668. <https://doi.org/10.1016/j.jechem.2024.05.023>.
- 24 Zou, X.; Xie, J.; Wang, C.; Jiang, G.; Tang, K.; Chen, C. *Chinese Chem. Lett.* **2023**, *34* (6), 107908. <https://doi.org/10.1016/j.ccl.2022.107908>.
- 25 Fang, J.-Y.; Fan, J.-L.; Liu, S.-B.; Sun, S.-P.; Lou, Y.-Y. *Materials (Basel)*. **2023**, *16* (11), 4000. <https://doi.org/10.3390/ma16114000>.
- 26 Xie, L.; Wang, Y.; Kong, Q.; Cao, R. *ChemCatChem* **2024**, *16* (21), e202400956. <https://doi.org/10.1002/cctc.202400956>.
- 27 Yu, Z.; Gu, M.; Wang, Y.; Li, H.; Chen, Y.; Wei, L. *Adv. Energy Sustain. Res.* **2024**, *5* (5), 2300284. <https://doi.org/10.1002/aesr.202300284>.
- 28 Liang, J.; Li, Z.; Zhang, L.; He, X.; Luo, Y.; Zheng, D.; Wang, Y.; Li, T.; Yan, H.; Ying, B.; Sun, S.; Liu, Q.; Hamdy, M. S.; Tang, B.; Sun, X. *Chem* **2023**, *9* (7), 1768–1827. <https://doi.org/10.1016/j.chempr.2023.05.037>.
- 29 Li, T.; Tang, C.; Guo, H.; Wu, H.; Duan, C.; Wang, H.; Zhang, F.; Cao, Y.; Yang, G.; Zhou, Y. *ACS Appl. Mater. Interfaces* **2022**, *14* (44), 49765–49773. <https://doi.org/10.1021/acscami.2c14215>.
- 30 Li, T.; Tang, C.; Guo, H.; Yang, J.; Zhang, F.; Yang, G.; Zhou, Y. *Chem. Eng. J.* **2024**, *485*, 149560. <https://doi.org/10.1016/j.cej.2024.149560>.
- 31 Liu, Q.; Liu, Q.; Xie, L.; Yue, L.; Li, T.; Luo, Y.; Li, N.; Tang, B.; Yu, L.; Sun, X. *Chem. Commun.* **2022**, *58* (33), 5160–5163. <https://doi.org/10.1039/d2cc00611a>.
- 32 Chen, G.-F.; Yuan, Y.; Jiang, H.; Ren, S.-Y.; Ding, L.-X.; Ma, L.; Wu, T.; Lu, J.; Wang, H. *Nat. Energy* **2020**, *5* (8), 605–613. <https://doi.org/10.1038/s41560-020-0654-1>.
- 33 Hou, Z.; Cui, C.; Li, Y.; Gao, Y.; Zhu, D.; Gu, Y.; Pan, G.; Zhu, Y.; Zhang, T. *Adv. Mater.* **2023**, *35* (39), 2209876. <https://doi.org/10.1002/adma.202209876>.
- 34 Herklotz, A.; Lee, D.; Guo, E. J.; Meyer, T. L.; Petrie, J. R.; Lee, H. N. *J. Phys. Condens. Matter* **2017**, *29* (49), 493001. <https://doi.org/10.1088/1361-648X/aa949b>.
- 35 Fang, L.; Wang, S.; Song, C.; Lu, S.; Yang, X.; Qi, X.; Liu, H. *Chem. Eng. J.* **2022**, *446*, 137341. <https://doi.org/10.1016/j.cej.2022.137341>.
- 36 Qin, Y.; Yu, T.; Deng, S.; Zhou, X.-Y.; Lin, D.; Zhang, Q.; Jin, Z.; Zhang, D.; He, Y.-B.; Qiu, H.-J.; He, L.; Kang, F.; Li, K.; Zhang, T.-Y. *Nat. Commun.* **2022**, *13* (1), 3784. <https://doi.org/10.1038/s41467-022-31468-0>.
- 37 Li, J.; Zhan, G.; Yang, J.; Quan, F.; Mao, C.; Liu, Y.; Wang, B.; Lei, F.; Li, L.; Chan, A. W. M.; Xu, L.; Shi, Y.; Du, Y.; Hao, W.; Wong, P. K.; Wang, J.; Dou, S.-X.; Zhang, L.; Yu, J. C. *J. Am. Chem. Soc.* **2020**, *142* (15), 7036–7046. <https://doi.org/10.1021/jacs.0c00418>.
- 38 Liu, S.; Miao, W.; Ma, K.; Teng, H.; Zhang, X.; Li, J.; Li, W.; Cui, X.; Jiang, L. *Appl. Catal. B Environ. Energy* **2024**, *350*, 123919. <https://doi.org/10.1016/j.apcatb.2024.123919>.
- 39 Wu, J.; Yu, Y.-X. *Catal. Sci. Technol.* **2021**, *11* (21), 7160–7170. <https://doi.org/10.1039/d1cy01217g>.
- 40 Zhang, X.; Zhang, Q.; Peng, Y.; Ma, X.; Fan, G. *Int. J. Hydrogen Energy* **2022**, *47* (12), 7793–7801. <https://doi.org/10.1016/j.ijhydene.2021.12.122>.
- 41 Chen, F.-Y.; Wu, Z.-Y.; Gupta, S.; Rivera, D. J.; Lambeets, S. V.; Pecaut, S.; Kim, J. Y. T.; Zhu, P.; Finfrock, Y. Z.; Meira, D. M.; King, G.; Gao, G.; Xu, W.; Cullen, D. A.; Zhou, H.; Han, Y.; Perea, D. E.; Muhich, C. L.; Wang, H. *Nat. Nanotechnol.* **2022**, *17* (7), 759–767. <https://doi.org/10.1038/s41565-022-01121-4>.
- 42 Duan, T.; Chen, Y.; Wen, Q.; Duan, Y. *RSC Adv.* **2015**, *5* (25), 19601–19612. <https://doi.org/10.1039/c5ra01876e>.
- 43 Rajaramanan, T.; Natarajan, M.; Ravirajan, P.; Senthilnathanan, M.; Velauthapillai, D. *Ruthenium (Ru) Energies* **2020**, *13* (7), 1532. <https://doi.org/10.3390/en13071532>.
- 44 Lim, M.; Ma, Z.; O'Connell, G.; Yuwono, J. A.; Kumar, P.; Jalili, R.; Amal, R.; Daiyan, R.; Lovell, E. C. *Small* **2024**, *20* (33), 2401333. <https://doi.org/10.1002/sml.202401333>.
- 45 Ma, Z.; Tsounis, C.; Toe, C. Y.; Kumar, P. V.; Subhash, B.; Xi, S.; Yang, H. Y.; Zhou, S.; Lin, Z.; Wu, K. H.; Wong, R. J.; Thomsen, L.; Bedford, N. M.; Lu, X.; Ng, Y. H.; Han, Z.; Amal, R. *ACS Catal.*



- 2022, 12 (9), 4792–4805. <https://doi.org/10.1021/acscatal.1c05431>.
- 46 Li, P. X.; Qu, L.-M.; Zhang, C.-H.; Ren, X.-B.; Wang, H.-X.; Zhang, J.-L.; Mu, Y.-W.; Lü, B.-L. *J. Fuel Chem. Technol.* **2021**, *49* (10), 1558–1566. [https://doi.org/10.1016/S1872-5813\(21\)60154-8](https://doi.org/10.1016/S1872-5813(21)60154-8).
- 47 Chen, H.; Ma, Y.; Han, Y.; Mao, X.; Hu, Y.; Zhao, X.; Dong, Q.; Wen, B.; Du, A.; Wang, X.; Lyu, X.; Jia, Y. *Small* **2024**, *20* (26), 2309689. <https://doi.org/10.1002/smll.202309689>.
- 48 Fu, Y. Y.; Wang, R. M.; Xu, J.; Chen, J.; Yan, Y.; Narlikar, A. V.; Zhang, H. *Chem. Phys. Lett.* **2003**, *379* (3–4), 373–379. <https://doi.org/10.1016/j.cplett.2003.08.061>.
- 49 Morgan, D. J. *X-Ray Photoelectron Spectroscopy (XPS): An Introduction*; 2014. [http://sites.cardiff.ac.uk/xpsaccess/files/2014/07/AccessXPS\\_Primer\\_Paper.pdf](http://sites.cardiff.ac.uk/xpsaccess/files/2014/07/AccessXPS_Primer_Paper.pdf).
- 50 Liang, X.; Wang, X.; Zhang, X.; Lin, S.; Ji, M.; Liu, Q.; Wang, M. *ACS Catal.* **2024**, *14* (7), 4648–4655. <https://doi.org/10.1021/acscatal.4c00016>.
- 51 Liu, C.; Zhang, G.; Zhang, W.; Gu, Z.; Zhu, G. *Proc. Natl. Acad. Sci.* **2023**, *120* (3), e2209979120. <https://doi.org/10.1073/pnas>.
- 52 Frankcombe, T. J.; Liu, Y. *Chem. Mater.* **2023**, *35* (14), 5468–5474. <https://doi.org/10.1021/acs.chemmater.3c00801>.
- 53 Biesinger, M. C.; Payne, B. P.; Grosvenor, A. P.; Lau, L. W. M.; Gerson, A. R.; Smart, R. S. C. *Appl. Surf. Sci.* **2011**, *257* (7), 2717–2730. <https://doi.org/10.1016/j.apsusc.2010.10.051>.
- 54 Bernal Romero, J.; Chavez, O.; Rodriguez, C.; Gonzalez, S.; Fregoso, J.; Carbajal, V.; Clavel, G.; Hudak, O.; Cheng, J.; Tandoc, J.; Brown, J.; Gao, L. *MRS Adv.* **2024**, *9* (15), 1176–1182. <https://doi.org/10.1557/s43580-024-00866-5>.
- 55 Rahul, R.; Singh, R. K.; Bera, B.; Devivaraprasad, R.; Neergat, M. *Phys. Chem. Chem. Phys.* **2015**, *17* (23), 15146–15155. <https://doi.org/10.1039/c5cp00692a>.
- 56 Antunes, V. G.; Figueroa, C. A.; Alvarez, F. *Langmuir* **2022**, *38* (6), 2109–2116. <https://doi.org/10.1021/acs.langmuir.1c03189>.
- 57 Kim, Y.; Watanabe, M.; Matsuda, J.; Song, J. T.; Takagaki, A.; Staykov, A.; Ishihara, T. *Appl. Catal. B Environ.* **2020**, *278*, 119292. <https://doi.org/10.1016/j.apcatb.2020.119292>.
- 58 Nasiri-Tabrizi, B. *J. Adv. Ceram.* **2014**, *3* (1), 31–42. <https://doi.org/10.1007/s40145-014-0090-4>.
- 59 Craciun, F.; Galassi, C.; Birjega, R. *J. Appl. Phys.* **2012**, *112* (12). <https://doi.org/10.1063/1.4770326>.
- 60 Li, J.; Wu, X. L.; Hu, D. S.; Yang, Y. M.; Qiu, T.; Shen, J. C. *Solid State Commun.* **2004**, *131* (1), 21–25. <https://doi.org/10.1016/j.ssc.2004.04.026>.
- 61 Perenlei, G.; Talbot, P. C.; Martens, W. N.; Riches, J.; Alarco, J. A. *RSC Adv.* **2017**, *7* (26), 15632–15643. <https://doi.org/10.1039/c6ra27633d>.
- 62 Sun, Y.; Ren, Y.; Liu, Y.; Wen, J.; Okasinski, J. S.; Miller, D. J. *Nat. Commun.* **2012**, *3*, 6–11. <https://doi.org/10.1038/ncomms1963>.
- 63 Lei, Q.; Huang, L.; Yin, J.; Davaasuren, B.; Yuan, Y.; Dong, X.; Wu, Z. P.; Wang, X.; Yao, K. X.; Lu, X.; Han, Y. *Nat. Commun.* **2022**, *13* (1), 4857. <https://doi.org/10.1038/s41467-022-32601-9>.
- 64 Fan, Q.; Yan, P.; Liu, F.; Xu, Z.; Liang, P.; Cao, X.; Ye, C.; Liu, M.; Zhao, L.; Ren, S.; Miao, H.; Zhang, X.; Yang, Z.; Ding, X.; Yang, J.; Kong, C.; Wu, Y. *Sci. Bull.* **2024**, *69* (18), 2881–2891. <https://doi.org/10.1016/j.scib.2024.06.031>.
- 65 Zaza, F.; Orio, G.; Serra, E.; Caprioli, F.; Pasquali, M. In *AIP Conference Proceedings*; 2015; Vol. 1667, p 1. <https://doi.org/10.1063/1.4922560>.
- 66 Biswas, M.; Misra, D.; Kundu, T. K. *Eur. Phys. J. B* **2023**, *96* (6), 74. <https://doi.org/10.1140/epjb/s10051-023-00547-6>.
- 67 Duan, J.; Zhao, Y.; Wu, Y.; Liu, Y.; Chen, J.; Yang, R.; Huang, J.; Luo, C.; Wu, M.; Zheng, X.; Li, P.; Jiang, X.; Guan, J.; Zhai, T. *Chem. Sci.* **2024**, *15*, 19546–19555. <https://doi.org/10.1039/d4sc05873a>. DOI: 10.1039/D5TA09764A
- 68 Wen, W.; Yan, P.; Sun, W.; Zhou, Y.; Yu, X.-Y. *Adv. Funct. Mater.* **2023**, *33* (6), 2212236. <https://doi.org/10.1002/adfm.202212236>.
- 69 Zhang, R.; Shang, S.; Wang, F.; Chu, K. *Dalt. Trans.* **2024**, *53* (8), 3470–3475. <https://doi.org/10.1039/d4dt00043a>.
- 70 Huang, K.; Tang, K.; Wang, M.; Wang, Y.; Jiang, T.; Wu, M. *Adv. Funct. Mater.* **2024**, *34* (24), 2315324. <https://doi.org/10.1002/adfm.202315324>.
- 71 Geng, J.; Ji, S. *Nano Res.* **2024**, *17* (6), 4898–4907. <https://doi.org/10.1007/s12274-024-6480-1>.
- 72 Zhao, C.; Tan, G.; Yang, W.; Xu, C.; Liu, T.; Su, Y.; Ren, H.; Xia, A. *Sci. Rep.* **2016**, *6* (1), 38603. <https://doi.org/10.1038/srep38603>.
- 73 Platt, P.; Mella, R.; DeMaio, W.; Preuss, M.; Wenman, M. R. *Comput. Mater. Sci.* **2017**, *140*, 322–333. <https://doi.org/10.1016/j.commatsci.2017.09.001>.
- 74 Cao, H.; Wang, G.; Zhang, L.; Liang, Y.; Zhang, S.; Zhang, X. *ChemPhysChem* **2006**, *7* (9), 1897–1901. <https://doi.org/10.1002/cphc.200600130>.
- 75 Chourpa, I.; Douziech-Eyrolles, L.; Ngaboni-Okassa, L.; Fouquenot, J. F.; Cohen-Jonathan, S.; Soucé, M.; Marchais, H.; Dubois, P. *Analyst* **2005**, *130* (10), 1395–1403. <https://doi.org/10.1039/b419004a>.
- 76 Phu, N. D.; Ngo, D. T.; Hoang, L. H.; Luong, N. H.; Chau, N.; Hai, N. H. *J. Phys. D: Appl. Phys.* **2011**, *44* (34). <https://doi.org/10.1088/0022-3727/44/34/345002>.
- 77 De Faria, D. L. A.; Venâncio Silva, S.; De Oliveira, M. T. J. *Raman Spectrosc.* **1997**, *28* (11), 873–878. [https://doi.org/10.1002/\(sici\)1097-4555\(199711\)28:11<873::aid-jrs177>3.0.co;2-b](https://doi.org/10.1002/(sici)1097-4555(199711)28:11<873::aid-jrs177>3.0.co;2-b).
- 78 Bhalerao, G. M.; Singh, M. K.; Sinha, A. K.; Ghosh, H. *Phys. Rev. B - Condens. Matter Mater. Phys.* **2012**, *86* (12), 125419. <https://doi.org/10.1103/PhysRevB.86.125419>.
- 79 Davydov, S. Y.; Posrednik, O. V. *Phys. Solid State* **2021**, *63* (4), 530–533. <https://doi.org/10.1134/S1063783421040053>.
- 80 Xiang, H.; Liu, W.; Su, L.; Chen, S.; Han, Y.; Zhu, C.; Wang, S.; Tan, C.; Zhang, L. *Sep. Purif. Technol.* **2024**, *330*, 125357. <https://doi.org/10.1016/j.seppur.2023.125357>.
- 81 Lim, M.; Sun, J.; Ma, Z.; Jalili, R.; Daiyan, R.; Lovell, E. C.; Amal, R. *ACS Appl. Nano Mater.* **2023**, *6* (6), 4936–4945. <https://doi.org/10.1021/acsnm.3c00681>.
- 82 Zhu, M. K.; Lu, P. X.; Hou, Y. D.; Song, X. M.; Wang, H.; Yan, H. *J. Am. Ceram. Soc.* **2006**, *89* (12), 3739–3744. <https://doi.org/10.1111/j.1551-2916.2006.01281.x>.
- 83 Yuan, Z.; Sohn, H. Y. *ISIJ Int.* **2014**, *54* (6), 1235–1243. <https://doi.org/10.2355/isijinternational.54.1235>.
- 84 Fu, W.; Hu, Z.; Zheng, Y.; Su, P.; Zhang, Q.; Jiao, Y.; Zhou, M. *Chem. Eng. J.* **2022**, *433*, 133680. <https://doi.org/10.1016/j.cej.2021.133680>.
- 85 Fang, J.-Y.; Zheng, Q.-Z.; Lou, Y.-Y.; Zhao, K.-M.; Hu, S.-N.; Li, G.; Akdim, O.; Huang, X.-Y.; Sun, S.-G. *Nat. Commun.* **2022**, *13* (1), 7899. <https://doi.org/10.1038/s41467-022-35533-6>.
- 86 Chu, K.; Luo, Y.; Shen, P.; Li, X.; Li, Q.; Guo, Y. *Adv. Energy Mater.* **2022**, *12* (3), 2103022. <https://doi.org/10.1002/aenm.202103022>.
- 87 Barbosa, A. I.; Costa Lima, S. A.; Reis, S. *Molecules* **2019**, *24* (2), 346. <https://doi.org/10.3390/molecules24020346>.
- 88 Al-Abduly, A.; Christensen, P. *Plasma Sources Sci. Technol.* **2015**, *24* (6), 065006. <https://doi.org/10.1088/0963-0252/24/6/065006>.
- 89 Han, S.; Li, H.; Li, T.; Chen, F.; Yang, R.; Yu, Y.; Zhang, B. *Nat. Catal.* **2023**, *6* (5), 402–414. <https://doi.org/10.1038/s41929-023-00951-2>.
- 90 Alenazi, N.; Hussein, M.; Alamry, K.; Asiri, A. A Real Sample Analysis. *J. Carbon Res.* **2018**, *4* (2), 30. <https://doi.org/10.3390/c4020030>.



- 91 Karelin, A. I.; Kayumov, R. R.; Dobrovolsky, Y. A. *Spectrochim. Acta Part A Mol. Biomol. Spectrosc.* **2019**, *215*, 381–388. <https://doi.org/10.1016/j.saa.2019.03.007>.
- 92 Verma, S. K.; Deb, M. K. *Anal. Chim. Acta* **2007**, *582* (2), 382–389. <https://doi.org/10.1016/j.aca.2006.09.020>.
- 93 Søndergaard, T.; Cleemann, L. N.; Zhong, L.; Becker, H.; Steenberg, T.; Hjuler, H. A.; Seerup, L.; Li, Q.; Jensen, J. O. *Electrocatalysis* **2018**, *9* (3), 302–313. <https://doi.org/10.1007/s12678-017-0427-1>.
- 94 Katipamula, S.; White, N. M.; Waldie, K. M. *Chem Catal.* **2023**, *3* (3), 100561. <https://doi.org/10.1016/j.checat.2023.100561>.
- 95 Zhang, X.; Liu, X.; Huang, Z.-F.; Guo, L.; Gan, L.; Zhang, S.; Ajmal, M.; Pan, L.; Shi, C.; Zhang, X.; Yang, G.; Zou, J. *JACS Catal.* **2023**, *13* (22), 14670–14679. <https://doi.org/10.1021/acscatal.3c04541>.
- 96 Murphy, E.; Sun, B.; Rüscher, M.; Liu, Y.; Zang, W.; Guo, S.; Chen, Y. H.; Hejral, U.; Huang, Y.; Ly, A.; Zhenyuk, I. V.; Pan, X.; Timoshenko, J.; Cuenya, B. R.; Spoerke, E. D.; Atanassov, P. *Adv. Mater.* **2024**, *36* (27), 2401133. <https://doi.org/10.1002/adma.202401133>.
- 97 Wang, Y.; Xia, S.; Cai, R.; Zhang, J.; Wang, J.; Yu, C.; Cui, J.; Zhang, Y.; Wu, J.; Yang, S.; Tan, H. H.; Wu, Y. *Small* **2023**, *19* (26), 2302295. <https://doi.org/10.1002/smll.202302295>.
- 98 Choi, S. R.; Lim, M.; Kim, D. Y.; An, W. Y.; Lee, S. W.; Choi, S.; Bae, S. J.; Yim, S. D.; Park, J. Y. *Int. J. Hydrogen Energy* **2022**, *47* (39), 17379–17392. <https://doi.org/10.1016/j.ijhydene.2022.03.222>.
- 99 Luo, W.; Guo, Z.; Ye, L.; Wu, S.; Jiang, Y.; Xu, P.; Wang, H.; Qian, J.; Zhou, X.; Tang, H.; Ge, Y.; Guan, J.; Yang, Z.; Nie, H. *Small* **2024**, *20* (30), 2311336. <https://doi.org/10.1002/smll.202311336>.
- 100 Li, Y.; Wang, C.; Yang, L.; Ge, W.; Shen, J.; Zhu, Y.; Li, C. *Adv. Energy Mater.* **2024**, *14* (7), 2303863. <https://doi.org/10.1002/aenm.202303863>.
- 101 Penetrante, B. M.; Hsiao, M. C.; Merritt, B. T.; Vogtlin, G. E. 1997; Vol. 106. <https://doi.org/10.4271/971715>.
- 102 McLarnon, C. R.; Penetrante, B. M. 1998. <https://doi.org/10.4271/982434>.
- 103 Ding, Z.; Wang, K.; Mai, Z.; He, G.; Liu, Z.; Tang, Z. *Int. J. Hydrogen Energy* **2019**, *44* (45), 24680–24689. <https://doi.org/10.1016/j.ijhydene.2019.07.244>.
- 104 Wang, M.; Ji, S.; Wang, H.; Wang, X.; Linkov, V.; Ma, X.; Wang, R. *J. Alloys Compd.* **2023**, *948*, 169713. <https://doi.org/10.1016/j.jallcom.2023.169713>.
- 105 Wang, H.; Wang, M.; Wang, J. *Curr. Chinese Sci.* **2023**, *3* (3), 204–212. <https://doi.org/10.2174/2210298103666221102092735>.
- 106 Lei, F.; Li, K.; Yang, M.; Yu, J.; Xu, M.; Zhang, Y.; Xie, J.; Hao, P.; Cui, G.; Tang, B. *Inorg. Chem. Front.* **2022**, *9* (11), 2734–2740. <https://doi.org/10.1039/d2qi00489e>.
- 107 Fan, X.; Zhao, D.; Deng, Z.; Zhang, L.; Li, J.; Li, Z.; Sun, S.; Luo, Y.; Zheng, D.; Wang, Y.; Ying, B.; Zhang, J.; Alshehri, A. A.; Lin, Y.; Tang, C.; Sun, X.; Zheng, Y. *Small* **2023**, *19* (17), 2208036. <https://doi.org/10.1002/smll.202208036>.
- 108 Ramadhany, P.; Trần-Phú, T.; Yuwono, J.A.; Hocking, R.K.; Ma, Z.; Ta, X.M.C.; Kumar, P.; Gunawan, D.; Johannessen, B.; Tricoli, A.; Simonov, A.N.; Amal, R.; Daiyan, R.; *Nat. Commun.* **2026**, *17*, 1776. <https://www.nature.com/articles/s41467-026-68481-6>
- 109 Ma, Z.; Leverett, J.; Yuwono, J. A.; Pan, J.; Zhou, S.; Zhang, D.; Zhang, M.; Xie, B.; Peng, L.; Khan, M. H. A.; Londono, S. L.; Kumar, Priyank V.K.; Lovell, E.; Daiyan, R.; Amal, R. *Chem. Eng. J.* **2025**, *524*, 168996. <https://doi.org/10.1016/j.cej.2025.168996>
- 110 Blöchl, P. E. *Phys. Rev. B* **1994**, *50* (24), 17953–17979. <https://doi.org/10.1103/PhysRevB.50.17953>.
- 111 Kresse, G.; Joubert, D. *Phys. Rev. B* **1999**, *59* (3), 1758–1775. <https://doi.org/10.1103/PhysRevB.59.1758>.
- 112 Kresse, G.; Furthmüller, J. *Phys. Rev. B* **1996**, *54* (16), 11169–11186. <https://doi.org/10.1103/PhysRevB.54.11169>
- 113 Kresse, G.; Furthmüller, J. *Comput. Mater. Sci.* **1996**, *6* (1), 15–50. [https://doi.org/10.1016/0927-0256\(96\)00008-0](https://doi.org/10.1016/0927-0256(96)00008-0).
- 114 Perdew, J. P.; Burke, K.; Ernzerhof, M. *Phys. Rev. Lett.* **1996**, *77* (18), 3865–3868. <https://doi.org/10.1103/PhysRevLett.77.3865>.
- 115 Cardenas-Flechas, L. J.; Barba-Ortega, J. J.; Joya, M. R. *Ceramica* **2022**, *68* (385), 52–59. <https://doi.org/10.1590/0366-69132022683853152>.



The data supporting this article have been included as part of the Supplementary Information. Supplementary information: Figures S1-S24 and Tables S1-S3. See DOI: [URL – format <https://doi.org/DOI>]

[View Article Online](#)

DOI: 10.1039/D5TA09764A

